Article

Longitudinal molecular trajectories of diffuse glioma in adults

https://doi.org/10.1038/s41586-019-1775-1

Received: 8 February 2019

Accepted: 1 October 2019

Published online: 20 November 2019

Floris P. Barthel[1,2,72], Kevin C. Johnson[1,72], Frederick S. Varn[1], Anzhela D. Moskalik[1], Georgette Tanner[3], Emre Kocakavuk[1,4,5], Kevin J. Anderson[1], Olajide Abiola[1], Kenneth Aldape[6], Kristin D. Alfaro[7], Donat Alpar[8,9], Samirkumar B. Amin[1], David M. Ashley[10], Pratiti Bandopadhayay[11,12], Jill S. Barnholtz-Sloan[13], Rameen Beroukhim[12,14], Christoph Bock[8,15], Priscilla K. Brastianos[16], Daniel J. Brat[17], Andrew R. Brodbelt[18], Alexander F. Bruns[3], Ketan R. Bulsara[19], Aruna Chakrabarty[20], Arnab Chakravarti[21], Jeffrey H. Chuang[1,22], Elizabeth B. Claus[23,24], Elizabeth J. Cochran[25], Jennifer Connelly[26], Joseph F. Costello[27], Gaetano Finocchiaro[28], Michael N. Fletcher[29], Pim J. French[30], Hui K. Gan[31,32], Mark R. Gilbert[33], Peter V. Gould[34], Matthew R. Grimmer[27], Antonio Iavarone[35,36,37], Azzam Ismail[20], Michael D. Jenkinson[18], Mustafa Khasraw[38], Hoon Kim[1], Mathilde C. M. Kouwenhoven[39], Peter S. LaViolette[40], Meihong Li[1], Peter Lichter[29], Keith L. Ligon[12,41], Allison K. Lowman[40], Tathiane M. Malta[42], Tali Mazor[27], Kerrie L. McDonald[43], Annette M. Molinaro[27], Do-Hyun Nam[44,45], Naema Nayyar[16], Ho Keung Ng[46], Chew Yee Ngan[1], Simone P. Niclou[47], Johanna M. Niers[39], Houtan Noushmehr[42], Javad Noorbakhsh[1], D. Ryan Ormond[48], Chul-Kee Park[49], Laila M. Poisson[50], Raul Rabadan[51,52], Bernhard Radlwimmer[29], Ganesh Rao[53], Guido Reifenberger[54], Jason K. Sa[45], Michael Schuster[8], Brian L. Shaw[16], Susan C. Short[3], Peter A. Sillevis Smitt[30], Andrew E. Sloan[55,56,57], Marion Smits[58], Hiromichi Suzuki[59], Ghazaleh Tabatabai[60], Erwin G. Van Meir[61], Colin Watts[62], Michael Weller[63], Pieter Wesseling[2,64], Bart A. Westerman[65], Georg Widhalm[66], Adelheid Woehrer[67], W. K. Alfred Yung[7], Gelareh Zadeh[68], Jason T. Huse[69,70], John F. De Groot[7], Lucy F. Stead[3], Roel G. W. Verhaak[1]* & The GLASS Consortium[71]

The evolutionary processes that drive universal therapeutic resistance in adult patients with diffuse glioma remain unclear[1,2]. Here we analysed temporally separated DNA-sequencing data and matched clinical annotation from 222 adult patients with glioma. By analysing mutations and copy numbers across the three major subtypes of diffuse glioma, we found that driver genes detected at the initial stage of disease were retained at recurrence, whereas there was little evidence of recurrence-specific gene alterations. Treatment with alkylating agents resulted in a hypermutator phenotype at different rates across the glioma subtypes, and hypermutation was not associated with differences in overall survival. Acquired aneuploidy was frequently detected in recurrent gliomas and was characterized by IDH mutation but without co-deletion of chromosome arms 1p/19q, and further converged with acquired alterations in the cell cycle and poor outcomes. The clonal architecture of each tumour remained similar over time, but the presence of subclonal selection was associated with decreased survival. Finally, there were no differences in the levels of immunoediting between initial and recurrent gliomas. Collectively, our results suggest that the strongest selective pressures occur during early glioma development and that current therapies shape this evolution in a largely stochastic manner.

Diffuse glioma is the most common malignant brain tumour in adults and invariably relapse despite treatment with surgery, radiotherapy and chemotherapy. The molecular landscape of glioma at diagnosis has been extensively characterized[3–9]. Although these efforts have led to the identification of driver genes and clinically relevant subtypes[10,11], how the glioma genetic landscape evolves over time and in response to therapy is unknown.

Intratumoral heterogeneity is a well-recognized characteristic of gliomas and results from selective pressures such as a limited availability of nutrients, clonal competition and treatment[12–15]. Tumours are thought to circumvent these growth bottlenecks by dynamic competition of subclones that result in the most favourable environment for tumour sustenance[1]. Recent studies have suggested that stochastic changes in clone frequency (that is, neutral evolution) and immune surveillance

A list of affiliations appears at the end of the paper.

may further contribute to the observed intratumoral heterogeneity[16,17]. An understanding of evolutionary dynamics at several time points is needed to develop strategies aimed at delaying or preventing the onset of tumour progression.

To investigate clonal dynamics over time and in response to therapeutic pressures, we established the Glioma Longitudinal Analysis (GLASS) Consortium. GLASS is a community-driven effort that seeks to overcome the logistical challenges in constructing adequately powered longitudinal genomic glioma datasets by pooling datasets from patients treated at institutions worldwide[18]. We have analysed longitudinal profiles across the three molecular glioma subtypes to identify the molecular processes active at initial and recurrent time points. These analyses identified few common features of glioma evolution across subtypes, and instead pointed towards highly variable and patient-specific trajectories of genomic alterations.

GLASS cohort

We pooled existing and newly generated longitudinal DNA sequencing datasets from 288 patients treated at 35 hospitals (Supplementary Table 1, Extended Data Fig. 1). After applying quality filters, tumour samples from 222 patients with high-quality data in at least two time points were classified according to molecular markers into three major glioma subtypes: (1) IDH-mutant and chromosome 1p/19q co-deleted (hereafter referred to as IDH-mutant-codel; $n = 25$); (2) IDH-mutant without co-deletion of chromosome 1p/19q (hereafter IDH-mutant-noncodel; $n = 63$); and (3) IDH-wild-type ($n = 134$), in alignment with the World Health Organization (WHO) classification of tumours of the central nervous system[10,11]. For each patient, we selected two time-separated tumour samples, henceforth termed initial and recurrence, for further analysis.

Mutational burdens and processes over time

We first evaluated temporal changes in mutational burden and processes to understand general patterns of glioma evolution. Mutation burdens in initial tumours were comparable with previously reported rates[6,7,19]. There were 2.20 mutations (single-nucleotide variants and small insertions or deletions) per megabase (Mb) for IDH-mutant-codels; 2.52 mutations per Mb for IDH-mutant-noncodels; and 2.85 mutations per Mb for IDH-wild-type glioma (Fig. 1a, Extended Data Fig. 2a). Excluding DNA hypermutation cases (more than 10 mutations per Mb, $n = 35$), the mutation burden increased after recurrence in 70% of the cohort (Extended Data Fig. 2a). To study changes during tumour progression, we separated mutations into three fractions: initial only, recurrence only, or shared. Notably, the mutation burdens of the private fractions, but not the shared fraction, were comparable between subtypes (Extended Data Fig. 2b). Patient age at diagnosis was significantly associated with the shared mutational burden ($P = 1.7 \times 10^{-7}$), and to a lesser extent with the burden of mutations private to the initial tumour ($P = 0.0256$) (Extended Data Fig. 2c). On average, a longer time to recurrence was associated with a larger increase in mutation burden ($P = 0.0043$, Extended Data Fig. 2d).

These fraction-specific differences in mutational burden suggested that the activity of distinct mutational processes may also be time-dependent. We therefore classified mutations in each fraction according to the Catalogue of Somatic Mutations in Cancer (COSMIC) signature database[20]. As expected, signature activity was closely related to subtype and fraction (Fig. 1b, Extended Data Fig. 3a). Signature 1 (ageing) was nearly always the dominant signature among shared mutations in IDH-wild-type tumours, whereas the shared fraction in IDH-mutant-noncodel and IDH-mutant-codel tumours—tumour subtypes that are associated with a younger age of diagnosis—also showed a strong presence of signature 16 (unknown aetiology). Signatures 3 (double-strand break repair), 15 (mismatch repair) and 8 (unknown aetiology) were mostly confined to the private fractions, which suggests that these processes were of lesser importance to tumour maintenance than those associated with ageing.

The treatment of glioma includes alkylating agents that can induce hypermutations after treatment[21–23]. We observed enrichment of the associated signature 11 in recurrent tumours treated with alkylating agents and with a mutational load exceeding 10 mutations per Mb (Fig. 1a, Extended Data Fig. 3b). Treatment-associated hypermutation occurred most frequently among IDH-mutant-noncodels (47%), followed by IDH-mutant-codels (25%), and IDH-wild-type gliomas (16%) (Fig. 1c). The proportion of hypermutation events was significantly different between the three glioma subtypes (Fisher's exact test $P = 2.0 \times 10^{-3}$), which suggests that IDH-mutant-noncodels are most sensitive to developing a hypermutator phenotype[24].

Treatment-induced hypermutation has been associated with disease progression[23]. We did not find any differences in overall survival between hypermutators and non-hypermutators treated with alkylating agents independent of age, subtype and *MGMT* methylation status (Fig. 1d, Supplementary Table 2a, b). To assess the pathogenicity of acquired mutations further, we studied their clonality[25]. Newly acquired clonal mutations have penetrated most of the tumour (that is, a selective sweep) between initial and recurrence and mark clonal expansion[26]. Conversely, acquired subclonal mutations are less prevalent, and therefore less likely to drive disease progression. Previous reports have suggested that mutations associated with alkylating agents are frequently clonal[27]. We found that in 48% of hypermutated tumours, most of the recurrence-only mutations were clonal, potentially reflecting cases in which a selective sweep occurred (Extended Data Fig. 4a). However, IDH-mutant-noncodel hypermutators with predominantly clonal mutations did not show differences in survival compared with those containing predominantly subclonal mutations (log-rank test $P = 0.38$, Extended Data Fig. 4b). Alkylating agents such as temozolomide prolong the survival of adult patients with glioma[28,29]. Our results show that treatment-induced hypermutation is common across subtypes and does not associate with reduced overall survival, supporting the noted benefit of alkylating agent therapy.

Selective pressures during glioma evolution

Environmental and treatment-induced pressures may drive changes in clonal architecture at recurrence. To evaluate selection over time, we clustered copy number changes and mutations on the basis of their cancer cell fraction (CCF). CCF values represent the fraction of cancer cells that contain a given alteration and reflect the relative timing of events, because alterations that are present in a subset of cancer cells probably occurred later than events present in all cancer cells (Fig. 2a). Most tumours (84%) demonstrated a mutational cluster with a CCF greater than 50% that persisted from the initial tumour to recurrence, probably reflecting the tumour trunk and containing the tumour-initiating driver mutations[30] (Fig. 2b, Extended Data Fig. 5a). To determine changes in clonal dominance over time, we ranked clusters within each sample by their CCF value and found similarities in clonal architecture throughout the course of disease (Kendall rank correlation, tau = 0.20, $P = 3.76 \times 10^{-24}$; Fig. 2b, Extended Data Fig. 5b–d). These results suggested that the clonal structure at initial disease mostly persisted into recurrence.

To deepen our assessment of selective pressures, we evaluated selection in initial and recurrent tumours by determining the normalized ratio between non-synonymous and synonymous mutations (dN/dS)[31]. Higher ratios (above one) suggest positive selection, and ratios less than one suggest negative selection. We found evidence for positive selection at both time points despite differences between subtypes (Fig. 2c). Separating mutations into mutational fractions demonstrated that shared but not private mutations showed positive dN/dS ratios in all three glioma subtypes, which indicates that only shared

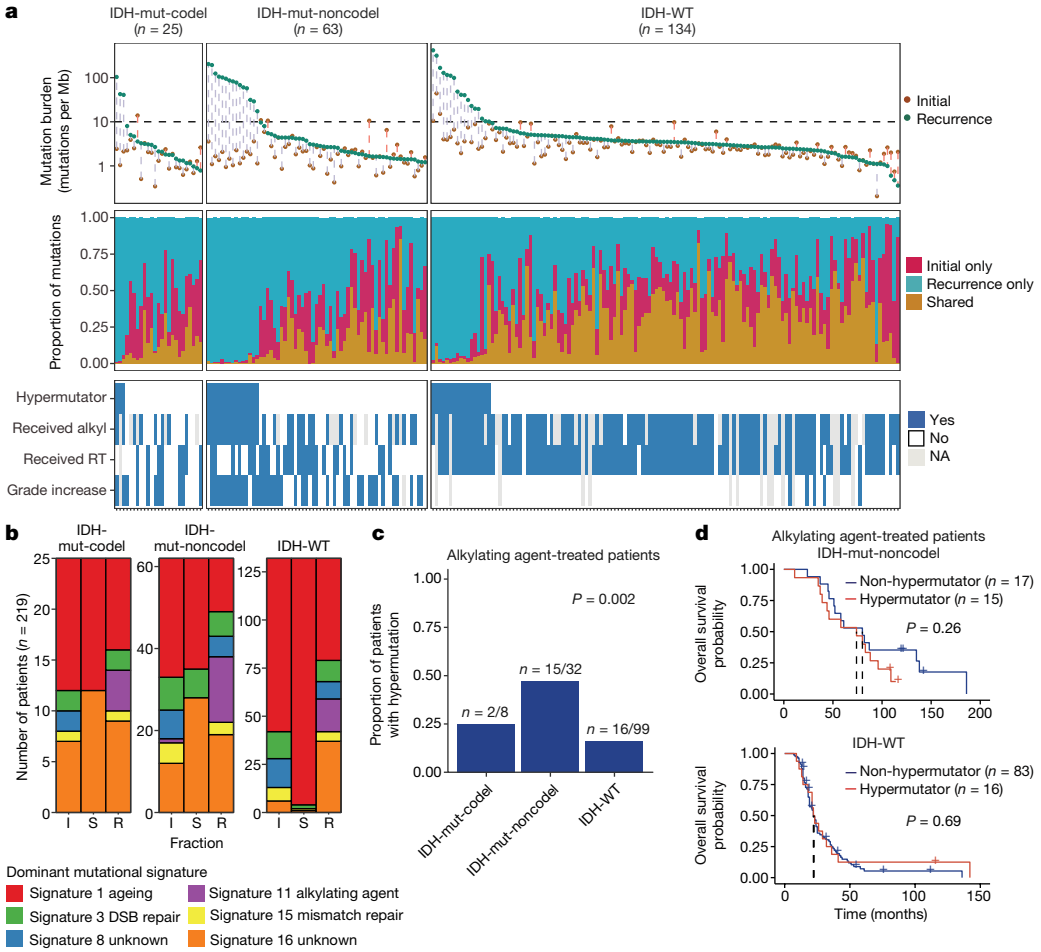

Fig. 1 | Temporal changes in glioma mutational burden and processes. **a**, Each column represents a single patient ($n = 222$) at two separate time points grouped by glioma subtype and ordered left-to-right by decreasing mutation frequency at recurrence. Top, mutation frequency differences between initial and recurrent tumours. Blue dotted line indicates increased mutation frequency, and the red dotted line indicates decreased mutational frequency. Middle, the proportion of total mutations shared (mustard), private to initial (magenta), or private to recurrence (blue). Bottom, clinical information including hypermutation status, therapy and grade changes. RT, radiation therapy. Alkyl, alkylating agent. **b**, Stacked bar plot ($n = 219$) indicating the dominant mutational signature among initial, recurrent and shared mutation fractions stratified by glioma subtype. I, initial; S, shared; R, recurrence. **c**, The proportion of glioma recurrences with alkylating agent-related hypermutation, grouped by glioma subtype. Fisher's exact test was used to compare proportions between subtypes. **d**, Kaplan–Meier curve depicting overall survival in hypermutant (red) versus non-hypermutant (blue) patients treated with alkylating agent among IDH-wild-type (left, $n = 99$) and IDH-mutant-noncodel (right, $n = 32$) tumours. *P* values determined by log-rank test.

mutations (including truncal mutations) are likely to be subject to positive selection (Fig. 2c). The dN/dS ratio of initial-only mutations showed that these are neither positively nor negatively selected for, whereas recurrence-only mutations were subject to negative selection in IDH-wild-type gliomas.

To verify the reduced selective pressure in the private mutations, we used an orthogonal method to test for evidence of selection[32]. The method uses distributions of variant allele frequencies and estimated mutation rates to detect whether profiles significantly deviate from a model of neutral evolution (that is, as depicted by a linear relationship in Fig. 2d). In accordance with results of the dN/dS ratios, private mutations demonstrated dynamics that were consistent with neutral evolution (Fig. 2d). Shared subclonal mutations deviated from linearity and were consistent with selection both in non-hypermutators and hypermutators (Fig. 2d, Extended Data Fig. 6a, b), which provides further evidence that the strongest selective forces occur early in gliomagenesis.

Cohort-level analysis of selection masks the heterogeneity that exists in individual evolutionary trajectories. To determine the selective effects at each tumour time point, we used a Bayesian framework (SubClonalSelection algorithm) that simultaneously provides sample-specific probabilities for both selection and neutrality while modelling sources of noise in sequencing data. The classification of a sample as 'selection' or 'neutral' is determined by whichever model has the greater probability. Classification as neutral reflects the accumulation of random mutations that are not subject to selection. Given the stringent algorithm requirements, 183 patients were included in this analysis with at least one time point, and 104 patients with both time points (16 IDH-mutant-codels, 29 IDH-mutant-noncodels, 59 IDH-wild-type; Supplementary Table 3). Neutral-to-neutral was the most common evolutionary trajectory across all three subtypes (52%), and IDH-wild-type tumours displayed the highest observed selection at any time point, with selection detected in 64% of tumours (Fisher's exact test $P = 0.01$; Fig. 2e, Supplementary Table 3). IDH-wild-type gliomas with evidence for selection at recurrence had a shorter overall survival than IDH-wild-type gliomas classified as neutral at recurrence ($P = 0.027$; log-rank statistic, Fig. 2f), which suggests that subclonal competition associates with more aggressive tumour behaviour. To address the limitations of smaller sample sizes in the IDH-mutant subtypes, we performed a Cox proportional hazards model including age at first diagnosis, all three glioma subtypes, and mode of selection at recurrence. This analysis revealed that selection at recurrence was significantly

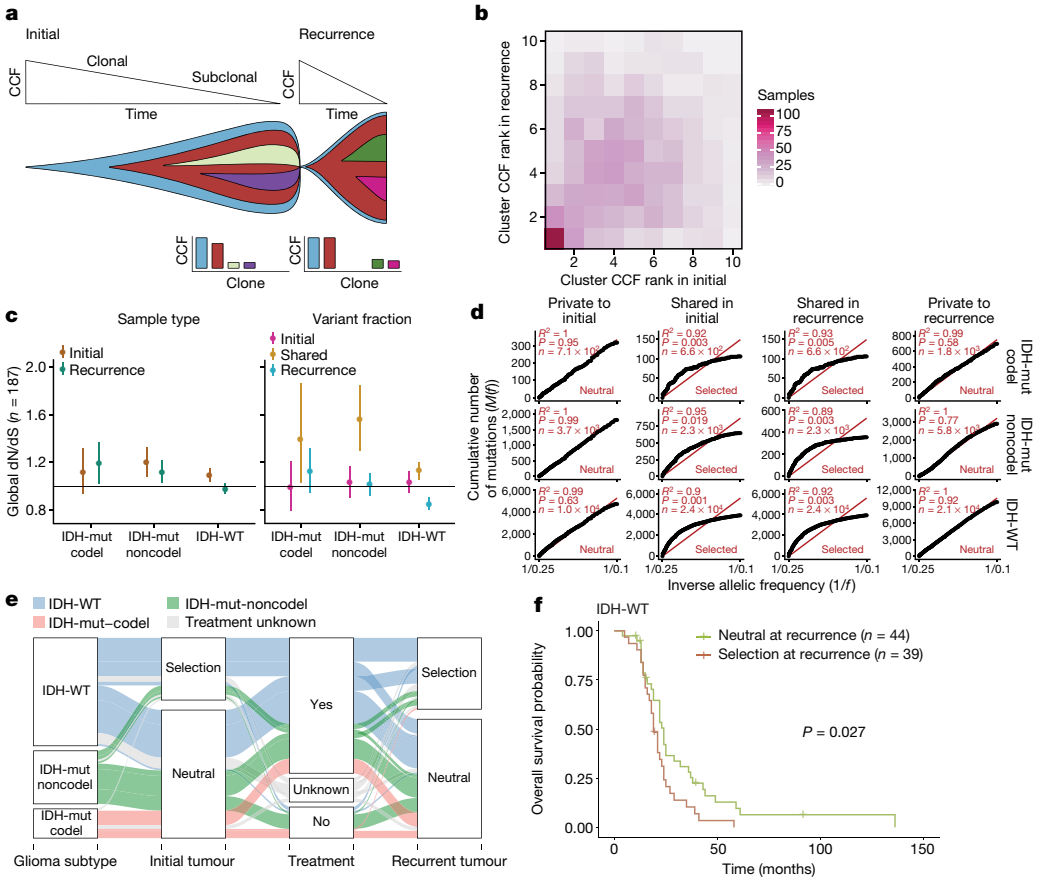

Fig. 2 | Quantifying selective pressures during glioma evolution. **a**, Schematic depiction of CCF values during tumour evolution indicating clonality and associated relative timing. **b**, Comparison of PyClone clusters ranked by CCF in matched initial and recurrent tumours. **c**, Left, dN/dS ratio for all variants (that is, global) in initial and recurrent tumours for each subtype. Hypermutators were not included ($n = 187$). Dots represent the global dN/dS ratio with associated Wald confidence intervals. Right, global dN/dS ratios for variant fractions per subtype. **d**, Cumulative distribution of subclonal mutations by their inverse variant allele frequency. Mutations were separated by time point, variant fraction and glioma subtype. Deviation from a linear relationship, significant Kolmogorov–Smirnov P values and Pearson's R^2 values below 0.98 indicate selection. **e**, Sankey plot indicating the breakdown of SubClonalSelection evolutionary modes by subtype and therapy ($n = 104$). The sizes of the bands reflect sample sizes and band colours highlight the glioma subtype. Grey colouring reflects instances when treatment information was not available. **f**, Kaplan–Meier curve showing survival differences between IDH-wild-type recurrent tumours demonstrating selection ($n = 39$) compared with neutrally evolving tumours ($n = 44$). P value determined by log-rank test.

associated with shorter survival across subtypes (Hazard ratio = 1.53, 95% confidence interval 1.00–2.41, $P = 0.048$; Supplementary Table 4). We next investigated whether radiation and chemotherapy imposed a selective effect, by comparing the evolutionary status at recurrence with treatment and other clinical variables. We did not observe significant associations between subclonal selection and radiation therapy or chemotherapy (Fisher's exact test $P > 0.05$; Supplementary Table 5), which suggests that standard therapeutic approaches for glioma have limited effect on the subclonal tumour architecture. Although high-depth sequencing datasets may be required to detect subtle selective effects[26], our analyses raise the possibility that the survival benefit derived from standard chemoradiation results from the elimination of tumour cells in which treatment sensitivity of individual cells is not determined by genetic factors.

Driver alteration frequencies across time

We evaluated how stability, acquisition and the loss of mutation and copy number drivers[6] over time affect glioma evolution. We used the dN/dS ratio to nominate 12 candidate mutation driver genes at both time points ($Q < 0.05$, Fig. 3a, Extended Data Fig. 7a) and determined significant alterations in copy number that recapitulated previously identified drivers (Extended Data Fig. 7b). Mutations in *IDH1* and co-occurring loss of the 1p/19q chromosome arms have been suggested as glioma-initiating events[1], which was corroborated by the observation that these events were not lost or acquired during the surgical interval (Fig. 3a, Extended Data Fig. 8a). Similarly, we observed that mutations in the *TERT* promoter were almost always shared in the IDH-mutant-codel and IDH-wild-type samples, although many samples lacked sufficient coverage in this GC-rich region. Chromosome 7 gains and chromosome 10 losses were present in a large majority of IDH-wild-type initial tumours and persisted into recurrence.

Shifts in the fraction of cancer cells containing an event may also indicate a time dependency of drivers. We determined changes in cellular prevalence of shared driver events by ordering events in each sample by their CCF value (Extended Data Fig. 9). *ATRX* mutations in IDH-mutant-noncodel initial tumours demonstrated lower CCFs than *TP53* ($P = 0.03$) and *IDH1* ($P = 0.10$) mutations, suggesting that *IDH1* and *TP53* mutations precede *ATRX* inactivation[1]. There was no difference in CCF values between *IDH1* and *TP53* among initial gliomas ($P = 0.98$); however, *IDH1* mutations demonstrated significantly lower CCF values than *TP53* mutations ($P = 0.0018$) in recurrent gliomas. We did not observe any CCF differences among driver mutations detected in IDH-wild-type tumours at either time point. Chromosome 10 deletion CCFs were higher than chromosome 7 amplifications ($P = 0.0036$), which indicates that chromosome 10 deletions arise earlier[33]. Similarly,

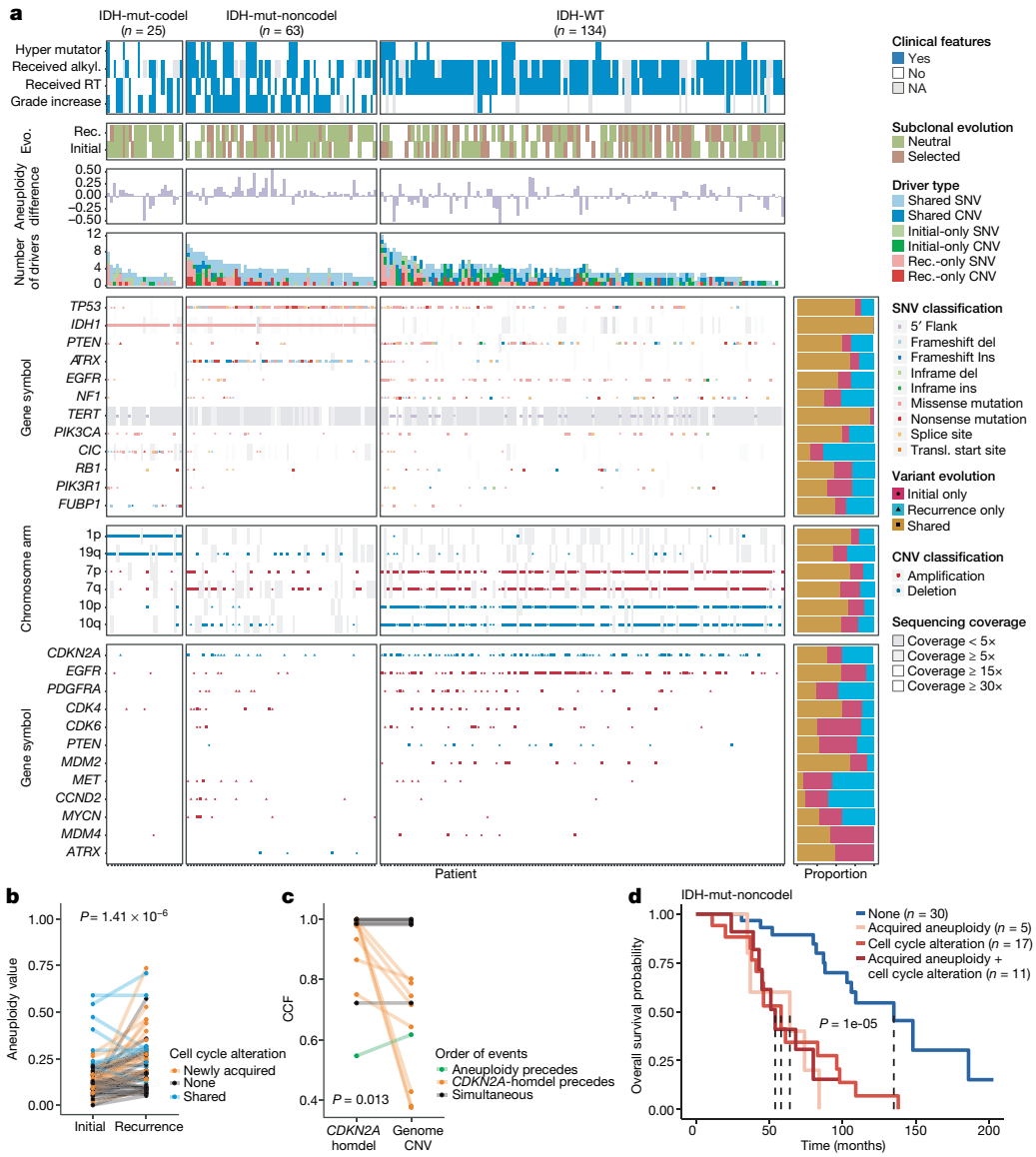

Fig. 3 | Patterns of glioma driver frequencies over time. a, Driver dynamics for single-nucleotide variants (SNVs) nominated by the dN/dS ratios and copy number alterations (CNVs) nominated by GISTIC ($n = 222$). Each column represents a single patient at two separate time points stratified by subtype and ordered left-to-right by the number of driver alterations. The degree of aneuploidy difference (recurrence − initial) offers a summary metric for increases (>0) or decreases (<0) in aneuploidy at recurrence. Variants are marked and different shapes indicate whether a variant was shared or private. The variant type is depicted by its colour. Stacked bar plots accompanying each gene/arm provide cohort-level proportions for whether the alteration was shared, lost or acquired. Rec, recurrence; evo, evolution. **b**, Aneuploidy comparison in matching initial and recurrent IDH-mutant-noncodel tumours. **c**, Within-sample CCF comparison of *CDKN2A* homozygous deletion (homdel) to genome-wide CCF as a proxy for aneuploidy. A relative higher CCF indicates temporal precedence. *P* value determined by Wilcoxon signed-rank test. **d**, Kaplan–Meier curve comparing survival in IDH-mutant-noncodel tumours with an alteration in the cell cycle, acquired aneuploidy, or both (shades of red) versus unaltered IDH-mutant-noncodel tumours (blue). *P* value determined by log-rank test.

there was no difference in CCF values between *CDKN2A* deletion and *EGFR* amplification ($P = 0.70$). *EGFR* and chromosomal arm events significantly differed (that is, 10p del versus *EGFR* amp, $P = 0.0019$) but not *CDKN2A* deletion and chromosomal events (that is, 10p del versus CDKN2A del, $P = 0.33$). The consistently high CCF values for *EGFR* amplifications could indicate that these events precede even some larger chromosomal aberrations, while not excluding the possibility that high levels of extrachromosomal *EGFR*[34] artificially inflate CCF.

Longitudinal changes in CCF values provide additional insights into evolutionary dynamics. For instance, the CCF value may increase when a driver event is linked to clonal expansion, or conversely, decrease when a clone is outcompeted. Most individual drivers did not demonstrate significant consistent CCF changes between the initial tumour and recurrence (Extended Data Fig. 10a). A notable exception was the *TP53* mutation CCF that increased over time ($P = 0.037$) in IDH-mutant-noncodels, but not IDH-wild-type gliomas ($P = 0.13$, Extended Data Fig. 10b). We did not observe any differences in *IDH1* CCF over time among IDH-mutant-noncodel tumours, possibly because the general trend of these tumours to increase in CCF is counteracted by the biological loss of relevance of mutant *IDH1* over time (Extended Data Fig. 10c). Indeed, a gross comparison of all shared mutation CCFs revealed an increase in recurrent IDH-mutant-noncodel tumours ($P < 0.0001$), which may reflect increased clonality and a reduction in intratumoral heterogeneity (Extended Data Fig. 10d). By contrast, shared CCFs decreased in IDH-wild-type tumours, potentially indicating a general increase in intratumoral heterogeneity at recurrence ($P < 0.0001$, Extended Data

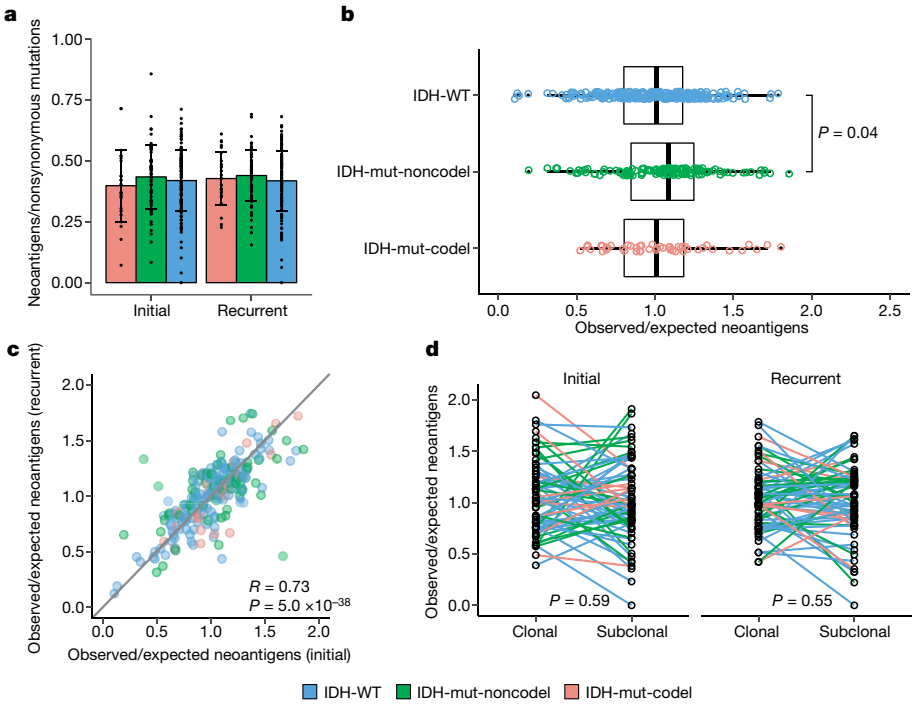

Fig. 4 | Neoantigen selection during tumour progression. a, Mean proportion of coding mutations giving rise to neoantigens (neoantigens/nonsynonymous mutations) stratified by glioma subtype and time point ($n = 222$). Data are mean ± s.d. **b**, Box plot depicting the distribution of observed-to-expected neoantigen ratios in the GLASS cohort stratified by glioma subtype. *P* value determined by *t*-test. Each box spans quartiles, with the lines representing the median ratio for each group. Whiskers represent absolute range, excluding outliers. **c**, Scatterplot depicting the association between the observed-to-expected neoantigen ratio in a patient's initial versus recurrent tumours. Each point represents a single patient tumour pair. *R* denotes Pearson correlation coefficient. Panels **b** and **c** only include samples from pairs with at least three neoantigens in the initial and recurrent tumours ($n = 131$, 63 and 24 pairs for IDH-wild-type, IDH-mutant-noncodel, and IDH-mutant-codel, respectively). **d**, Ladder plot depicting the difference in observed-to-expected neoantigen ratio between a tumour's clonal and subclonal neoantigens. Each set of points connected by a line represents one tumour. Tumours are stratified by whether they were a patient's initial or recurrent tumour. Lines are coloured by each patient's glioma subtype. Panel **d** only includes samples from pairs with at least three clonal neoantigens and at least three subclonal neoantigens in both the initial and recurrent tumours ($n = 35$, 20 and 9 for IDH-WT, IDH-mutant-noncodel and IDH-mutant-codel, respectively). *P* value determined by paired two-sided *t*-test. Colours in each panel represent the glioma subtype.

Fig. 10d). We confirmed that IDH-mutant-noncodel CCF increases and IDH-wild-type decreases were not biased by patients with high mutational burden through the classification of patient-specific shared mutation CCF change (Extended Data Fig. 10e).

We next investigated whether specific somatic alterations were acquired or lost over time. Gene-specific enrichment of many recurrence-only mutations was found in hypermutated tumours, but there was no enrichment for somatic gene alterations in non-hypermutators, which suggests that glioma recurrence is not directed by particular sets of mutations (Extended Data Fig. 8b). Within subtypes, we detected an enrichment in *CDKN2A* homozygous deletions (Fig. 3a, Extended Data Fig. 8a) in recurrent IDH-mutant-noncodels, which was corroborated by additional alterations to cell cycle genes (focal gain of *CCND2*, *CDK4* and *CDK6*, and mutation or homozygous loss of *RB1*). Mutations in cell cycle checkpoint control genes are associated with genomic instability[35]. Therefore, we analysed aneuploidy levels by determining the proportion of the genome that had undergone aneuploidy events (Extended Data Fig. 11a, b). We observed that IDH-mutant-noncodel tumours had a higher level of aneuploidy at recurrence (Wilcoxon rank sum test $P = 1.4 \times 10^{-6}$ total aneuploidy, $P = 8.6 \times 10^{-3}$ arm-level aneuploidy; Extended Data Fig. 11c, d) with tumours carrying acquired cell cycle gene alterations displaying the largest increases in aneuploidy ($P = 7.6 \times 10^{-6}$; Wilcoxon rank sum test, Fig. 3b). We reasoned that *CDKN2A* deletions may precede aneuploidy. Homozygous *CDKN2A* deletions had significantly higher CCFs than the average somatic copy number variation CCF across the genome (as a surrogate for aneuploidy-related copy number changes), suggesting that *CDKN2A* loss occurred before aneuploidy (Fig. 3c). These alterations may hasten disease progression as patients with either alterations in cell cycle genes or the largest increases in aneuploidy at recurrence demonstrated significantly shorter survival than patients without these alterations (log-rank test $P < 0.0001$, Fig. 3d). Together, the persistence of drivers over time and the paucity of consistent change indicate that therapy does not result in selection of specific sets of molecular changes.

Immunoediting activity in glioma

We next investigated how the immune microenvironment affects evolutionary trajectories. The immune system may prune tumour cells carrying immunogenic (neo-)antigens, resulting in the selection of subclones capable of evading the immune response. Evidence of this immunoediting process has been shown in several cancer types, including glioma[36–39], and suggests active immunosurveillance that may be therapeutically exploited[40]. We computationally predicted neoantigen-causing mutations[41]. As expected, the neoantigen load across the GLASS cohort was strongly correlated with exonic mutation burden (Spearman's rho = 0.89), with 42% of nonsynonymous exonic mutations giving rise to neoantigens on average. This fraction did not significantly differ by glioma subtype or between initial and recurrent tumours ($P > 0.05$, Wilcoxon rank-sum test; Fig. 4a). The most common neoantigen arose from the clonal R132H mutation in *IDH1* and was present in of 22 out of 88 IDH-mutant initial and recurrent tumours. Beyond mutations in *IDH1*, no mutations gave rise to a neoantigen found in more than three tumours at a given time point (Supplementary Table 6). Across the dataset, neoantigens and non-immunogenic mutations exhibited similar changes in CCF values between initial and

recurrent tumours indicating a lack of neoantigen-specific selection processes over time (Extended Data Fig. 12a).

We then examined the extent to which immunoediting occurred by comparing the observed neoantigen rate of each sample to an expected rate that was empirically derived from our dataset. The output of this approach is a normally distributed set of ratios centred at 1. Samples with an observed-to-expected neoantigen ratio less than 1 exhibit evidence of neoantigen depletion relative to the rest of the dataset, and thus are more likely to have been immunoedited. We found that none of the three glioma subtypes contained observed-to-expected ratios that significantly differed from 1 ($P > 0.05$, one sample *t*-test), although IDH-wild-type tumours exhibited significantly lower scores than IDH-mutant-noncodels (*t*-test, $P = 0.04$; Fig. 4b). We also did not observe an association between the observed-to-expected ratio and survival when adjusting for subtype and age (Wald test, $P > 0.05$), nor was there a difference between samples with neutral evolution dynamics compared to those exhibiting evidence of subclonal selection. When comparing samples longitudinally, we found that the observed-to-expected neoantigen ratio was strongly correlated between initial and recurrent tumours of each patient (Pearson's $R = 0.73$, $P = 5 \times 10^{-38}$), which suggests that the neoantigen depletion level in the recurrence reflects that of the initial tumour (Fig. 4c).

Immunoediting is most likely to take place in the tumours with high cytolytic activity and low levels of immunosuppressive activity[39]. Hypermutators, which have high loads of neoantigens, have previously been associated with highly cytolytic microenvironments[38]. However, we did not observe any differences in the observed-to-expected neoantigen ratio between hypermutated recurrent tumours and their initial counterparts, nor did we observe differences between hypermutated and non-hypermutated recurrent tumours, indicating that immunoediting activity is not related to the total number of mutations in a sample (Wilcoxon rank-sum test $P > 0.05$; Extended Data Fig. 12b). To more directly determine whether there were immunological factors associated with neoantigen depletion, we analysed CIBERSORT immune cell fractions from a subset of samples that had undergone expression profiling in a previous study ($n = 84$ from 42 tumour pairs)[38,42]. Initial tumours with an observed-to-expected neoantigen ratio greater than 1 exhibited significantly higher levels of $CD4^+$ T cells than those with a ratio less than 1, whereas recurrent tumours with a ratio greater than 1 exhibited significantly higher levels of macrophages and neutrophils, and significantly lower levels of plasma cells relative to those with ratio less than 1 ($P < 0.05$, Wilcoxon rank-sum test; Extended Data Fig. 12c).

Although we did not detect many factors associated with the observed-to-expected neoantigen ratio, we did observe that the ratio was significantly associated with the total number of unique HLA loci in a patient (Spearman's rho = 0.28, $P = 2 \times 10^{-9}$), reflecting similar findings in lung cancer[43]. This may bias analyses comparing the ratio across patients. To determine whether immunoediting varies over time in a patient-agnostic manner, we compared the observed-to-expected neoantigen ratio derived from the clonal mutations of a sample, which likely arose earlier in tumour evolution, to that derived from their subclonal mutations, which arose later. We did not observe a significant difference in the observed-to-expected neoantigen ratio of each patient's clonal and subclonal neoantigens, regardless of glioma subtype or whether the sample was an initial tumour or recurrence ($P > 0.05$, paired *t*-test; Fig. 4d). Together, these analyses suggest that neoantigens in glioma are not exposed to differing levels of selective pressure throughout their development.

Discussion

We reconstructed the evolutionary trajectories of 222 patients with glioma to help to understand treatment failures and tumour progression. The longitudinal molecular profiles revealed common features such as acquired hypermutation and aneuploidy, and also highlighted the individualistic paths of glioma evolution after treatment. Our results provide evidence that the current standard of care therapies do not frequently coerce glioma down predictable paths. Instead, an unexpected number of gliomas appeared to evolve stochastically after early driver events. We expect that continuing to profile patient tumours over time using comprehensive sequencing approaches will identify other common evolutionary paths. Our results highlight the prospects of several ongoing efforts that may inform new glioma therapies.

The observation that treatment-induced hypermutation occurred across subtypes, but did not confer a detrimental effect on patient survival, leaves the clinical importance of glioma hypermutation uncertain[21–24,27]. Future analyses that consider the number of therapy cycles and *MGMT* DNA methylation status will help to determine factors that predispose tumours to hypermutation and identify therapies that effectively exploit the vulnerabilities of this phenotype (for example, high mutational burden). Acquired cell cycle alterations and aneuploidy in recurrent IDH-mutant-noncodel gliomas also provide a rationale to target these more aggressive phenotypes with CDK inhibitors[44] or with compounds that disrupt microtubule dynamics[45]. Finally, our analyses revealed that immunoediting activity does not vary in glioma over time, although we did observe variation between individual patients. Further molecular and immunological data are needed to fully understand the effect that this variability has on glioma evolution and to devise therapies directed at the glioma immune response[17]. To this end, we found that clonal neoantigens arising from the IDH1(R132H) mutation persisted from the initial tumour into the recurrence, justifying neoantigen vaccine approaches as treatments for initial and recurrent glioma[46,47].

Collectively, these findings help shape our perspective on what constitutes an optimal treatment, and what approaches would result in the greatest removal or killing of glioma cells possible. Genomic characterization efforts such as The Cancer Genome Atlas (TCGA) have greatly increased our understanding of glioma biology but were limited to a single snapshot in evolutionary time. The GLASS resource provides a framework to study the patterns of glioma evolution and treatment response.

Online content

Any methods, additional references, Nature Research reporting summaries, source data, extended data, supplementary information, acknowledgements, peer review information; details of author contributions and competing interests; and statements of data and code availability are available at https://doi.org/10.1038/s41586-019-1775-1.

1. Barthel, F. P., Wesseling, P. & Verhaak, R. G. W. Reconstructing the molecular life history of gliomas. *Acta Neuropathol.* **135**, 649–670 (2018).
2. Osuka, S. & Van Meir, E. G. Overcoming therapeutic resistance in glioblastoma: the way forward. *J. Clin. Invest.* **127**, 415–426 (2017).
3. Bettegowda, C. et al. Mutations in CIC and FUBP1 contribute to human oligodendroglioma. *Science* **333**, 1453–1455 (2011).
4. Zheng, S. et al. A survey of intragenic breakpoints in glioblastoma identifies a distinct subset associated with poor survival. *Genes Dev.* **27**, 1462–1472 (2013).
5. Cancer Genome Atlas Research Network. Comprehensive genomic characterization defines human glioblastoma genes and core pathways. *Nature* **455**, 1061–1068 (2008).
6. Ceccarelli, M. et al. Molecular profiling reveals biologically discrete subsets and pathways of progression in diffuse glioma. *Cell* **164**, 550–563 (2016).
7. The Cancer Genome Atlas Research Network. Comprehensive, integrative genomic analysis of diffuse lower-grade gliomas. *N. Engl. J. Med.* **372**, 2481–2498 (2015).
8. Verhaak, R. G. et al. Integrated genomic analysis identifies clinically relevant subtypes of glioblastoma characterized by abnormalities in *PDGFRA*, *IDH1*, *EGFR*, and *NF1*. *Cancer Cell* **17**, 98–110 (2010).
9. Yan, H. et al. *IDH1* and *IDH2* mutations in gliomas. *N. Engl. J. Med.* **360**, 765–773 (2009).
10. Louis, D. N. et al. International Society of Neuropathology—Haarlem consensus guidelines for nervous system tumor classification and grading. *Brain Pathol.* **24**, 429–435 (2014).
11. Louis, D. N. et al. The 2016 World Health Organization Classification of Tumors of the Central Nervous System: a summary. *Acta Neuropathol.* **131**, 803–820 (2016).
12. Venteicher, A. S. et al. Decoupling genetics, lineages, and microenvironment in IDH-mutant gliomas by single-cell RNA-seq. *Science* **355**, eaai8478 (2017).
13. Patel, A. P. et al. Single-cell RNA-seq highlights intratumoral heterogeneity in primary glioblastoma. *Science* **344**, 1396–1401 (2014).

14. Snuderl, M. et al. Mosaic amplification of multiple receptor tyrosine kinase genes in glioblastoma. *Cancer Cell* **20**, 810–817 (2011).
15. Sottoriva, A. et al. Intratumor heterogeneity in human glioblastoma reflects cancer evolutionary dynamics. *Proc. Natl Acad. Sci. USA* **110**, 4009–4014 (2013).
16. Williams, M. J. et al. Quantification of subclonal selection in cancer from bulk sequencing data. *Nat. Genet*. **50**, 895–903 (2018).
17. Nejo, T. et al. reduced neoantigen expression revealed by longitudinal multiomics as a possible immune evasion mechanism in glioma. *Cancer Immunol. Res*. **7**, 1148–1161 (2019).
18. The GLASS Consortium. Glioma through the looking GLASS: molecular evolution of diffuse gliomas and the Glioma Longitudinal Analysis Consortium. *Neuro-oncol*. **20**, 873–884 (2018).
19. Hu, H. et al. Mutational landscape of secondary glioblastoma guides met-targeted trial in brain tumor. *Cell* **175**, 1665–1678.e1618 (2018).
20. Alexandrov, L. B. et al. Signatures of mutational processes in human cancer. *Nature* **500**, 415–421 (2013).
21. Wang, J. et al. Clonal evolution of glioblastoma under therapy. *Nat. Genet*. **48**, 768–776 (2016).
22. Kim, H. et al. Whole-genome and multisector exome sequencing of primary and post-treatment glioblastoma reveals patterns of tumor evolution. *Genome Res*. **25**, 316–327 (2015).
23. Johnson, B. E. et al. Mutational analysis reveals the origin and therapy-driven evolution of recurrent glioma. *Science* **343**, 189–193 (2014).
24. Hunter, C. et al. A hypermutation phenotype and somatic MSH6 mutations in recurrent human malignant gliomas after alkylator chemotherapy. *Cancer Res*. **66**, 3987–3991 (2006).
25. Jolly, C. & Van Loo, P. Timing somatic events in the evolution of cancer. *Genome Biol*. **19**, 95 (2018).
26. Turajlic, S., Sottoriva, A., Graham, T. & Swanton, C. Resolving genetic heterogeneity in cancer. *Nat. Rev. Genet*. **20**, 404–416 (2019).
27. Choi, S. et al. Temozolomide-associated hypermutation in gliomas. *Neuro-oncol*. **20**, 1300–1309 (2018).
28. Baumert, B. G. et al. Temozolomide chemotherapy versus radiotherapy in high-risk low-grade glioma (EORTC 22033-26033): a randomised, open-label, phase 3 intergroup study. *Lancet Oncol*. **17**, 1521–1532 (2016).
29. Buckner, J. C. et al. Radiation plus procarbazine, CCNU, and vincristine in low-grade glioma. *N. Engl. J. Med*. **374**, 1344–1355 (2016).
30. Yap, T. A., Gerlinger, M., Futreal, P. A., Pusztai, L. & Swanton, C. Intratumor heterogeneity: seeing the wood for the trees. *Sci. Transl. Med*. **4**, 127ps10 (2012).
31. Martincorena, I. et al. Universal patterns of selection in cancer and somatic tissues. *Cell* **171**, 1029–1041.e1021 (2017).
32. Williams, M. J., Werner, B., Barnes, C. P., Graham, T. A. & Sottoriva, A. Identification of neutral tumor evolution across cancer types. *Nat. Genet*. **48**, 238–244 (2016).
33. Korber, V. et al. Evolutionary trajectories of IDH(WT) glioblastomas reveal a common path of early tumorigenesis instigated years ahead of initial diagnosis. *Cancer Cell* **35**, 692–704.e612 (2019).
34. deCarvalho, A. C. et al. Discordant inheritance of chromosomal and extrachromosomal DNA elements contributes to dynamic disease evolution in glioblastoma. *Nat. Genet*. **50**, 708–717 (2018).
35. Giam, M. & Rancati, G. Aneuploidy and chromosomal instability in cancer: a jackpot to chaos. *Cell Div*. **10**, 3 (2015).
36. Marty, R., Thompson, W. K., Salem, R. M., Zanetti, M. & Carter, H. Evolutionary pressure against MHC class II binding cancer mutations. *Cell* **175**, 416–428.e413 (2018).
37. McGranahan, N. et al. Allele-specific HLA Loss and immune escape in lung cancer evolution. *Cell* **171**, 1259–1271.e1211 (2017).
38. Wang, Q. et al. Tumor evolution of glioma-intrinsic gene expression subtypes associates with immunological changes in the microenvironment. *Cancer Cell* **32**, 42–56.e46 (2017).
39. Rooney, M. S., Shukla, S. A., Wu, C. J., Getz, G. & Hacohen, N. Molecular and genetic properties of tumors associated with local immune cytolytic activity. *Cell* **160**, 48–61 (2015).
40. Dunn, G. P., Bruce, A. T., Ikeda, H., Old, L. J. & Schreiber, R. D. Cancer immunoediting: from immunosurveillance to tumor escape. *Nat. Immunol*. **3**, 991–998 (2002).
41. Hundal, J. et al. pVAC-Seq: A genome-guided in silico approach to identifying tumor neoantigens. *Genome Med*. **8**, 11 (2016).
42. Newman, A. M. et al. Robust enumeration of cell subsets from tissue expression profiles. *Nat. Methods* **12**, 453–457 (2015).
43. Rosenthal, R. et al. Neoantigen-directed immune escape in lung cancer evolution. *Nature* **567**, 479–485 (2019).
44. Raub, T. J. et al. Brain exposure of two selective dual CDK4 and CDK6 inhibitors and the antitumor activity of CDK4 and CDK6 inhibition in combination with temozolomide in an intracranial glioblastoma xenograft. *Drug Metab. Dispos*. **43**, 1360–1371 (2015).
45. van den Bent, M. et al. Efficacy of depatuxizumab mafodotin (ABT-414) monotherapy in patients with EGFR-amplified, recurrent glioblastoma: results from a multi-center, international study. *Cancer Chemother. Pharmacol*. **80**, 1209–1217 (2017).
46. Keskin, D. B. et al. Neoantigen vaccine generates intratumoral T cell responses in phase Ib glioblastoma trial. *Nature* **565**, 234–239 (2019).
47. Schumacher, T. et al. A vaccine targeting mutant IDH1 induces antitumour immunity. *Nature* **512**, 324–327 (2014).

[1]The Jackson Laboratory for Genomic Medicine, Farmington, CT, USA. [2]Department of Pathology, Brain Tumor Center Amsterdam, Amsterdam UMC, Vrije Universiteit Amsterdam, Amsterdam, The Netherlands. [3]Leeds Institute of Medical Research at St James's, University of Leeds, Leeds, UK. [4]DKFZ Division of Translational Neurooncology at the West German Cancer Center, German Cancer Consortium Partner Site, University Hospital Essen, Essen, Germany. [5]Department of Neurosurgery, University Hospital Essen, Essen, Germany. [6]Laboratory of Pathology, Center for Cancer Research, National Cancer Institute, Bethesda, MD, USA. [7]Department of Neuro-Oncology, The University of Texas MD Anderson Cancer Center, Houston, TX, USA. [8]CeMM Research Center for Molecular Medicine of the Austrian Academy of Sciences, Vienna, Austria. [9]1st Department of Pathology and Experimental Cancer Research, Semmelweis University, Budapest, Hungary. [10]Preston Robert Tisch Brain Tumor Center at Duke, Duke University Medical Center, Durham, NC, USA. [11]Department of Pediatric Oncology, Dana-Farber Cancer Institute, Boston, MA, USA. [12]Broad Institute, Cambridge, MA, USA. [13]Department of Population and Quantitative Health Sciences, Case Comprehensive Cancer Center, Case Western Reserve University School of Medicine, Cleveland, OH, USA. [14]Department of Medical Oncology, Dana-Farber Cancer Institute, Boston, MA, USA. [15]Department of Laboratory Medicine, Medical University of Vienna, Vienna, Austria. [16]Division of Neuro-Oncology, Massachusetts General Hospital, Boston, MA, USA. [17]Department of Pathology, Northwestern University Feinberg School of Medicine, Chicago, IL, USA. [18]Department of Neurosurgery, University of Liverpool & Walton Centre NHS Trust, Liverpool, UK. [19]Division of Neurosurgery, The University of Connecticut Health Center, Farmington, CT, USA. [20]Department of Cellular and Molecular Pathology, Leeds Teaching Hospital NHS Trust, St James's University Hospital, Leeds, UK. [21]Department of Radiation Oncology, The Ohio State Comprehensive Cancer Center–Arthur G. James Cancer Hospital, Columbus, OH, USA. [22]Department of Genetics and Genome Sciences, UConn Health, Farmington, CT, USA. [23]Yale University School of Public Health, New Haven, CT, USA. [24]Department of Neurosurgery, Brigham and Women's Hospital, Boston, MA, USA. [25]Department of Pathology & Laboratory Medicine, Medical College of Wisconsin, Milwaukee, WI, USA. [26]Department of Neurology, Medical College of Wisconsin, Milwaukee, WI, USA. [27]Department of Neurosurgery, University of California San Francisco, San Francisco, CA, USA. [28]Fondazione IRCCS Istituto Neurologico Besta, Milano, Italy. [29]Division of Molecular Genetics, Heidelberg Center for Personalized Oncology, German Cancer Research Consortium, German Cancer Research Center (DKFZ), Heidelberg, Germany. [30]Department of Neurology, Erasmus MC – University Medical Center Rotterdam, Rotterdam, The Netherlands. [31]Olivia Newton-John Cancer Research Institute, Austin Health, Melbourne, Victoria, Australia. [32]La Trobe University School of Cancer Medicine, Heidelberg, Victoria, Australia. [33]Neuro-Oncology Branch, National Institutes of Health, Bethesda, MD, USA. [34]Anatomic Pathology Service, Hôpital de l'Enfant-Jésus, CHU de Québec-Université Laval, Quebec, Quebec, Canada. [35]Department of Neurology, Columbia University Medical Center, New York, NY, USA. [36]Department of Pathology and Cell Biology, Columbia University Medical Center, New York, NY, USA. [37]Institute for Cancer Genetics, Columbia University Medical Center, New York, NY, USA. [38]Cooperative Trials Group for Neuro-Oncology (COGNO) NHMRC Clinical Trials Centre, The University of Sydney, Sydney, New South Wales, Australia. [39]Department of Neurology, Brain Tumor Center Amsterdam, Amsterdam UMC, Vrije Universiteit Amsterdam, Amsterdam, The Netherlands. [40]Department of Radiology, Medical College of Wisconsin, Milwaukee, WI, USA. [41]Department of Oncologic Pathology, Dana-Farber Cancer Institute, Boston, MA, USA. [42]Department of Neurosurgery, Henry Ford Health System, Henry Ford Cancer Institute, Detroit, MI, USA. [43]Cure Brain Cancer Biomarkers and Translational Research Group, Prince of Wales Clinical School, University of New South Wales, Sydney, New South Wales, Australia. [44]Department of Neurosurgery, Sungkyunkwan University School of Medicine, Samsung Medical Center, Seoul, South Korea. [45]Institute for Refractory Cancer Research, Samsung Medical Center, Seoul, South Korea. [46]Department of Anatomical and Cellular Pathology, The Chinese University of Hong Kong, Prince of Wales Hospital, Shatin, Hong Kong. [47]Department of Oncology, Luxembourg Institute of Health, Luxembourg, Luxembourg. [48]Department of Neurosurgery, University of Colorado School of Medicine, Aurora, CO, USA. [49]Department of Neurosurgery, Seoul National University College of Medicine, Seoul National University Hospital, Seoul, South Korea. [50]Department of Public Health Sciences, Henry Ford Health System, Henry Ford Cancer Institute, Detroit, MI, USA. [51]Department of Biomedical Informatics, Columbia University Medical Center, New York, NY, USA. [52]Department of Systems Biology, Columbia University, New York, NY, USA. [53]Department of Neurosurgery, The University of Texas MD Anderson Cancer Center, Houston, TX, USA. [54]Institute of Neuropathology, Heinrich Heine University Düsseldorf, Düsseldorf, Germany. [55]Department of Neurological Surgery, University Hospitals Cleveland Medical Center, Case Western Reserve University, Cleveland, OH, USA. [56]Department of Neurosurgery, Case Western Reserve University, Cleveland, OH, USA. [57]Seidman Cancer Center and Case Comprehensive Cancer Center, Case Western Reserve University, Cleveland, OH, USA. [58]Department of Radiology & Nuclear Medicine, Erasmus MC – University Medical Center Rotterdam, Rotterdam, The Netherlands. [59]The Hospital for Sick Children, Toronto, ON, Canada. [60]Interdiscplinary Division of Neuro-Oncology, Hertie Institute for Clinical Brain Research, DKTK Partner Site Tübingen, Eberhard Karls University Tübingen, Tübingen, Germany. [61]Department of Neurosurgery, School of Medicine and Winship Cancer Institute of Emory University, Atlanta, GA, USA. [62]Institute of Cancer Genome Sciences, Department of Neurosurgery, University of Birmingham, Birmingham, UK. [63]Department of Neurology, University Hospital Zurich, Zurich, Switzerland. [64]Princess Máxima Center for Pediatric Oncology, Utrecht, The Netherlands. [65]Department of Neurosurgery, Brain Tumor Center Amsterdam, Amsterdam UMC, Vrije Universiteit Amsterdam, Amsterdam, The Netherlands. [66]Department of Neurosurgery, Medical University of Vienna, Vienna, Austria. [67]Institute of Neurology, Medical University of Vienna, Vienna, Austria. [68]Division of Neurosurgery, Department of Surgery, University Health Network, Toronto, Ontario, Canada. [69]Department of Pathology, The University of Texas MD Anderson Cancer Center, Houston, TX, USA. [70]Department of Translational Molecular Pathology, The University of Texas MD Anderson Cancer Center, Houston, TX, USA. [71]A list of participants and their affiliations appears in the online version of the paper. [72]These authors contributed equally: Floris P. Barthel, Kevin C. Johnson. *e-mail: roel.verhaak@jax.org

The Glioma Longitudinal Analysis (GLASS) Consortium

Floris P. Barthel[1,2,72], Kevin C. Johnson[1,72], Frederick S. Varn[1], Anzhela D. Moskalik[1], Georgette Tanner[3], Emre Kocakavuk[1,4,5], Kevin J. Anderson[1], Kenneth Aldape[6], Kristin D. Alfaro[7], Samirkumar B. Amin[1], David M. Ashley[10], Pratiti Bandopadhayay[11,12], Jill S. Barnholtz-Sloan[13], Rameen Beroukhim[12,14], Christoph Bock[8,15], Priscilla K. Brastianos[16], Daniel J. Brat[17], Andrew R. Brodbelt[18], Ketan R. Bulsara[19], Aruna Chakrabarty[20], Jeffrey H. Chuang[1,22], Elizabeth B. Claus[23,24], Elizabeth J. Cochran[25], Jennifer Connelly[26], Joseph F. Costello[27], Gaetano Finocchiaro[28], Michael N. Fletcher[29], Pim J. French[30], Hui K. Gan[31,32], Mark R. Gilbert[33], Peter V. Gould[34], Antonio Iavarone[35,36,37], Azzam Ismail[20], Michael D. Jenkinson[18], Mustafa Khasraw[38], Hoon Kim[1], Mathilde C. M. Kouwenhoven[39], Peter S. LaViolette[40], Peter Lichter[29], Keith L. Ligon[12,41], Allison K. Lowman[40], Tathiane M. Malta[42], Kerrie L. McDonald[43], Annette M. Molinaro[27], Do-Hyun Nam[44,45], Ho Keung Ng[46], Simone P. Niclou[47], Johanna M. Niers[39], Houtan Noushmehr[42], D. Ryan Ormond[48], Chul-Kee Park[49], Laila M. Poisson[50], Raul Rabadan[51,52], Bernhard Radlwimmer[29], Ganesh Rao[53], Guido Reifenberger[54], Jason K. Sa[45], Susan C. Short[3], Peter A. Sillevis Smitt[30], Andrew E. Sloan[55,56,57], Marion Smits[58], Hiromichi Suzuki[59], Ghazaleh Tabatabai[60], Erwin G. Van Meir[61], Colin Watts[62], Michael Weller[63], Pieter Wesseling[2,64], Bart A. Westerman[65], Adelheid Woehrer[67], W. K. Alfred Yung[7], Gelareh Zadeh[68], Jason T. Huse[69,70], John F. De Groot[7], Lucy F. Stead[3] & Roel G. W. Verhaak[1]*

Methods

Data reporting

No statistical methods were used to predetermine sample size. The experiments were not randomized, and investigators were not blinded to allocation during experiments and outcome assessment.

DNA sequencing and data collection

The GLASS dataset consists of both unpublished and published sequencing data as outlined in Supplementary Table 1. Among the cohort were exomes from 436 glioma samples (200 patients), whole-genome data from 165 glioma samples (78 patients), with overlapping exome/whole-genome data on 78 glioma samples (38 patients). A matching germline sequence was available for all patients. The dataset includes 257 sets of at least two time-separated tumour samples, 17 standalone recurrences, and 19 patients with at least two geographically distinct tumour portions. More specifically, the dataset includes exome or whole-genome sequencing data on 211 primary gliomas, 234 first recurrences, 32 second recurrences, 11 third recurrences and 1 fourth recurrence (Supplementary Table 7).

Newly generated whole-genome sequencing data for the Chinese University of Hong Kong (HK), Northern Sydney Cancer Centre (NS) and MD Anderson Cancer Center (MD) cohorts were subjected to 150 base paired-end sequencing. The HK samples were sequenced using HiSeqX, whereas the NS and MD cohorts were sequenced using NovaSeq, according to Illumina's protocols. Whole-exome capture was performed using the following platforms as reported in previous publications[7,21–23,48–52].

The Agilent SureSelect Human All Exon 50 Mb capture kit was used for patients SF-0001–SF-0021, and the Agilent SureSelect Human All Exon V4 capture kit was used for patients SF-0024–SF-0029 in the University of California San Francisco cohort. The Agilent SureSelect Human All Exon v4 or v5 kit was used to capture samples in the Kyoto University cohort. The Samsung Medical Center cohort reported using the Agilent SureSelect kit for patients SM-R056–SM-R071, SM-R075, SM-R076 and SM-R095–SM-R114, whereas the Illumina TruSeq Exome-capture kit was used for patient SM-R072. Exome capture was performed using the Agilent SureSelect Human All Exon 50 Mb kit in the TCGA glioblastoma (GBM) cohort and the Agilent SureSelect Human All Exon v.2.0 44 Mb kit in the TCGA low grade glioma (LGG) cohort. Columbia University cases were captured using the Agilent V3 50 Mb kit, sequencing 90 bp paired-end reads for samples R009-TP, R009-R1, R011-TP, R011-R1, R014-TP, R014-R1, R017-R1, R018-R1 and R019-R1. Mapping files of initial tumour and normal samples of patients R017–R019 were obtained from the TCGA through the CG-hub. All other samples were captured using the Agilent SureSelect XT Human All Exon v.4 Kit, 80 million paired-end reads, 150× on-target coverage. Samples in the Henry Ford Hospital cohort were multiplexed and sequenced using Illumina HiSeq 2000 by the Sequencing and Microarray Facility at an average target exome coverage of 100× using 76-bp paired-end reads. Samples in the HK cohort were subjected to 75 base paired-end sequencing for HK-0001–HK-0004, as performed using NextSeq in high output mode. In the Leeds Cohort (LU), the SureSelectXT V5 kit (PE100) was used to construct exome libraries. The Illumina TruSeq Exome capture kit was used for samples at the Medical University of Vienna – Research Center for Molecular Medicine (CeMM).

GLASS identifiers

A GLASS barcode system was created, based on TCGA barcode design, in an effort to de-identify patient information and provide an organized framework for the different pieces of the dataset.

GLASS barcodes are composed of 24 characters. The first four characters specify the project (either GLSS or TCGA). All datasets submitted to The GLASS Consortium, published and unpublished, were given the GLSS project ID. Samples that were part of the TCGA cohorts (TCGA-GBM and TCGA-LGG) were given a TCGA designation. The next two characters designate the centre where the samples were either acquired or sequenced (Supplementary Table 7). This is followed by the four-character centre-specific patient identification that was kept as close as possible to the patient identification provided by the collaborators to allow a simplified trace-back process. Patient data are divided by a relative sample type, such as initial tumour (TP), recurrent tumour (R1), normal tissue (NB or NM, for example), or metastatic tumour sample (M1). If there was more than one recurrence the relative number was specified following 'R'. Some patients had surgeries for which a biospecimen was unavailable. Thus, a surgical number was also provided to indicate temporal ordering (Supplementary Table 8). To include spatially separated samples the portion designation was added, which is followed by one character specifying the type of analyte, either DNA (D) or RNA (R). As there is variation in the sequencing analysis, a three-character designation represents either whole-genome sequencing (WGS) or whole-exome sequencing (WXS). The last part of the GLASS barcode is a six-character designation unique to each barcode that was randomly generated.

Computational pipelines

All pipelines were developed using snakemake 5.2.2[53]. Unless otherwise stated, all tools mentioned are part of the GATK 4 suite[54]. All data were collected at a central location (The Jackson Laboratory) and analysed using homogenous pipelines capable of processing raw fastq files as well as re-processing previously analysed bam files.

Alignment and pre-processing

Data pre-processing was conducted in accordance to the GATK Best Practices using GATK 4.0.10.1. In brief, aligned BAM files were separated by read group, sanitized and stripped of alignments and attributes using 'RevertSam', giving one unaligned BAM (uBAM) file per readgroup. Uniform readgroups were assigned to uBAM files using 'AddOrReplaceReadgroups'. Similarly, unaligned fastq files were assigned uniformly designated readgroup attributes and converted to uBAM format using 'FastqToSam'. uBAM files underwent quality control using 'FastQC 0.11.7'. Sequencing adapters were marked using 'MarkIlluminaAdapters'. uBAM files were finally reverted to interleaved fastq format using 'SamToFastq', aligned to the b37 genome (human_g1k_v37_decoy) using 'BWA MEM 0.7.17', attributes were restored using 'MergeBamAlignment'. 'MarkDuplicates' was then used to merge aligned BAM files from multiple readgroups and to mark PCR and optical duplicates across identical sequencing libraries. Lastly, base recalibration was performed using 'BaseRecalibrator' followed by 'ApplyBQSR'. Coverage statistics were gathered using 'CollectWgsMetrics'. Alignment quality control was performed running 'ValidateSamFile' on the final BAM file and quality control results were inspected using 'MultiQC 1.6a0'[55]. A haplotype database for fingerprinting was generated using a modified version of the code on https://github.com/naumanjaved/fingerprint_maps. The tool 'CrosscheckFingerprints' was used to confirm that all readgroups within a sample belong to the same individual, and that all samples from one individual match. Any mismatches were marked and excluded from further analysis.

Variant detection

Variant detection was performed in accordance to the GATK Best practices using GATK 4.1.0.0. Germline variants were called from control samples using Mutect2 in artefact detection mode and pooled into a cohort-wide panel of normals. Somatic variants were subsequently called in individual tumour samples (single-sample mode) and in entire patients using GATK 4.1 Mutect2 in multi-sample mode. Mutect2 was given matched control samples, the aforementioned panel of normals and the gnomAD germline resource as additional controls. Cross-sample contamination was evaluated using 'GetPileupSummaries' and 'CalculateContamination' run for both tumour and matching control

samples. Read orientation artefacts were evaluated using 'CollectF1R2Counts' and 'LearnReadOrientationModel'. Somatic likelihood, read orientation, sequence context, germline and contamination filters were applied using 'FilterMutectCalls'.

Variant post-processing

BCFTools 1.9 was used to normalize, sort and index variants[56]. A consensus VCF was generated from all variants in the cohort, removing any duplicate variants. The consensus VCF file was annotated using GATK 4.1 Funcotator and the v1.6.20190124s annotation data source. Allele frequencies from multi-sample Mutect2 were used to compare allele frequencies between related samples. Multi-sample Mutect2 calls and filters mutations across a patient as a whole and does not determine mutation calls in a single sample. Single-sample mutation calls were overlaid on the multi-sample calls to infer whether variants were called in individual samples. Single-sample called variants that were not present in the multi-sample callset were discarded.

Mutational burden

Mutational burden was calculated as the number of mutations per Mb sequenced. A minimum coverage threshold of 15× was required for each base. DNA hypermutation was defined for recurrent tumours with greater than 10 mutations per Mb sequenced as these values were considered outliers (1.5 times the interquartile range above the upper quartile). Notably, there were a few initial gliomas that demonstrated a mutational frequency above 10 mutations per Mb. However, the 'hypermutation' classification was restricted to only patients with this level at recurrence since these likely reflect different evolutionary paths.

Mutational signatures

The relative contributions of the COSMIC mutational signatures were determined from a patient's initial-only, recurrence-only, and shared mutations by solving the non-negative-least squares problem for each set of mutations using the 30 signatures from version 2 (March 2015). Six signatures were dominantly enriched in at least 3% of the fractions and we resolved the non-negative-least squares problems using the reduced six-signature model to increase accuracy and reduce noise.

Copy number segmentation

Copy number identification was performed according to the GATK Best Practices and is outlined briefly here. The pipeline differs slightly for whole genomes and whole exomes. For whole genomes, the genome was segmented into 10kb bins using 'PreprocessIntervals'. For exomes, overlapping regions between several commonly used capture kits (Broad Human Exome b37, Nextera Rapid Capture, TruSeq Exome, SeqCap EZ Exome V3, Agilent SureSelect V4, Agilent SureSelect V7) were identified using 'bedtools multiIntersectBed'. The tool 'PreprocessIntervals' was used to apply 1-kb padding and to merge overlapping intervals. In parallel, 'SelectVariants' was used to subset the gnomAD resource of germline variants to variants with a population allele frequency greater than 5%. Next, 'CollectReadcounts' was used to count reads in the bins generated by 'PreprocessIntervals' separately for autosomes and allosomes. In parallel, 'CollectAllelicCounts' was used to count reference and alternate reads at gnomAD variant sites with a population allele frequency greater than 5%. The cohort was subsequently split into batches determined by sequencing centre and 'CreateReadCountPanelOfNormals' was used to create a panel of normal for each batch. Panel of normals were created separately for allosomes and autosomes, and allosomes were separated further by sex. To improve the panel of normals further, GC content annotation of each interval as determined by 'AnnotateIntervals' were given. Next, 'DenoiseReadCounts' was used to denoise the binned readcounts output by 'CollectReadCounts', given a panel of normal determined by batch, chromosomes (allosomes or autosomes) and sex. Denoised copy ratios were plotted and inspected for quality concerns using 'PlotDenoisedCopyRatios'. The tool 'ModelSegments' is an implementation of a gaussian-kernel binary-segmentation algorithm and was used to merge contiguous segments and assign copy and allelic ratios. The results of this segmentation were plotted using 'PlotModelledSegments' and inspected for quality concerns.

Copy number calling

A copy number caller loosely based on GATK 'CallCopyRatioSegments' (which in turn is based off of ReCapSeg) and GISTIC was implemented to call both arm-level and high-level copy number changes, respectively[57,58].

Segments (from 'ModelSegments') with a non-$\log_2$ copy ratio between 0.9 and 1.1 were determined to be neutral. These segments were then weighted by length and a weighted mean and standard deviation non-$\log_2$ copy ratio (once-filtered) were determined again. Outlier segments are removed and once again a weighted mean and standard deviation non-$\log_2$ copy ratio (twice-filtered) were determined. Segments with a non-$\log_2$ copy ratio between 0.9 and 1.1 and segments within two standard deviations of the twice-filtered mean were determined to be neutral, and segments outside of these boundaries were determined to have a low-level amplification or deletion, depending on the direction.

The weighted mean and standard deviation of the non-$\log_2$ copy ratio (once-filtered) was then determined individually for each chromosome arm. Outlier segments were removed and the weighted mean and standard deviation of the non-$\log_2$ copy ratio (twice-filtered) was determined again. To determine a high-level amplification and deletion threshold, the most highly amplified and deleted chromosome arms were selected, respectively. The twice-filtered mean plus (high level amplification) or minus (high level deletion) two times the standard deviation of the selected arms were used as high-level thresholds.

Gene level copy numbers were called by intersecting the gene boundaries with the segment intervals and by calculating the weighted non-$\log_2$ copy ratio for that gene. The copy number call for that gene was then determined by comparing the gene-level non-$\log_2$ copy ratio to the previously determined thresholds.

dNdScv

The dN/dS ratios were estimated using the R package dNdScv[31] (https://github.com/im3sanger/dndscv) was run using the default and recommended parameters for all mutations in initial tumour samples, recurrent tumour samples, and for each mutational fraction (unique to initial, unique to recurrent and shared). All analyses were conducted separately within the three main tumour subtypes.

Aneuploidy calculation

The most reductive metric of aneuploidy was computed by taking the size of all non-neutral segments divided by the size of all segments. The resulting aneuploidy value indicates the proportion of the segmented genome that is non-diploid.

In parallel, an arm-level aneuploidy score modelled after a previously described method was computed[59]. In brief, adjacent segments with identical arm-level calls (−1, 0 or 1) were merged into a single segment with a single call. For each merged/reduced segment, the proportion of the chromosome arm it spans was calculated. Segments spanning greater than 80% of the arm length resulted in a call of −1 (loss), 0 (neutral) or +1 (gain) to the entire arm, or 'NA' if no contiguous segment spanned at least 80% of the arm's length. For each sample the number of arms with a non-neutral event was finally counted. The resulting aneuploidy score is a positive integer with a minimum value of 0 (no chromosomal arm-level events detected) and a maximum value of 39 (total number of autosomal chromosome arms excluding the short arms for chromosomes 13, 14, 15, 21 and 22).

Estimates of evolutionary pressures

Evolutionary pressures were evaluated both by variant status and glioma subtype using the neutralitytestr algorithm as previously described (R package: neutralitytestr v.0.0.2, https://github.com/marcjwilliams1/neutralitytestr)[32]. Individual variant allele frequency vectors were merged at the level of glioma subtype by variant status. Only mutations found in copy-neutral regions were included in these analyses. For all else, default parameters were used. Merged variant allele frequency distributions were deemed to be selected when the neutral null hypothesis was rejected using several metrics. Tests for neutrality required that both $R^2 < 0.98$ and the area between the two curves of (1) merged variant allele frequency data and (2) a normalized distribution expected under neutrality to be significantly different.

The SubclonalSelection algorithm was applied to GLASS mutation data to measure the selection strength in individual tumour samples (Julia package: SubclonalSelection, https://github.com/marcjwilliams1/SubClonalSelection.jl)[16]. Patients that had samples at both time points with a TITAN-defined purity estimate ≥ 0.5 and ≥ 25 subclonal mutations in diploid regions were included. Mean coverage across all mutations was used as the 'read_depth' input parameter and the model was run with the recommended 10^6 iterations and 1,000 particles. Samples were classified as neutral or selected based on the model that had the highest probability, in line with the prior applications to TCGA data[16]. Classification based on the highest model probability yielded stable results as there was not a significant change in proportions when setting a higher classification probability threshold ($P > 0.05$, Pearson's chi-square test, for both probability thresholds of 0.6 and 0.7). At all three probability thresholds (0.5, 0.6 and 0.7), Kaplan–Meier survival analyses between selection at recurrence and overall survival continued to indicate that patients with IDH-wild-type tumours that were selected had a worse overall survival ($P = 0.03$ ($n = 81$), $P = 0.01$ ($n = 66$) and $P = 0.01$ ($n = 56$), respectively).

Mutation clonality

Each patient's clonal architecture was inferred using PyClone (v.0.13.1) by grouping SNVs into clonal clusters (https://github.com/aroth85/pyclone)[60]. The patient-level input mutation matrix was reduced by limiting to sites with at least 30× coverage across all samples. PyClone was subsequently run using a binomial density model, connected initiation, and 10,000 iterations. Sample purities were provided for each patient and parental copy number (minor and major allele counts) from TITAN were given. PyClone results were post-processed using a burn-in of 1,000, thin of 1, minimum cluster size of 2 and a maximum number of clusters per patient of 12. Individual mutations were determined to be clonal if the PyClone CCF values were ≥ 0.5, subclonal for mutations with CCF ≥ 0.1 and CCF < 0.5, mutations were considered non-clonal when CCF < 0.1, as previously described[61].

CNV clonality

Allele-specific copy number, tumour purity and ploidy estimates were derived using a probabilistic model (TITAN, v.1.19.1) for both whole-genome and whole-exome sequencing samples[62]. TITAN was supplied with the tumour denoised read counts output by GATK DenoiseReadCounts and the tumour allelic counts at loci found to be heterozygous in control samples output by ModelSegments. An 'alphaK' (and 'alphaKHigh') parameter of 2,500 and 10,000 was used for exomes and genomes, respectively. The patient sex was provided to improve fitting allosomes. For each tumour–control pair, TITAN was run assuming an initial ploidy of two or three, and assuming one to three clusters, resulting in a total of six possible solutions per tumour/control pair. To select the optimal solution, TITAN's internal selectSolution function was used with a threshold of 0.15 giving additional weight to diploid solutions.

Timing analysis

The CCF values output by TITAN or PyClone were used for separately timing copy number changes or mutations. To time specific copy number changes in genes, the average CCF for that gene was calculated. When timing mutations in genes, the highest CCF amongst the nonsynonymous mutations was taken.

Neoantigen analyses

Neoantigens in this analysis were defined as all 8–11-mer peptides that arose from an exonic nonsynonymous SNV or indel and bound their respective patient's HLA class I molecules at a binding affinity score (half-maximal inhibitory concentration, IC_{50}) that was ≤ 500 nM and better than or equal to the wild-type form of the peptide. Each patient's four-digit HLA class I types were inferred using OptiType (v.1.3.1, https://github.com/FRED-2/OptiType) run on each patient's matched normal sample[63]. VCF files for each tumour sample were annotated using Variant Effect Predictor (ensembl) with the 'downstream' and 'wildtype' plugins. Neoantigens from these VCFs were then called using pVACseq (v.4.0.10, https://github.com/griffithlab/pVAC-Seq)[41] run using netMHCpan (v.2.8, http://www.cbs.dtu.dk/services/NetMHCpan-2.8/)[64]. For each pVACseq run, epitope length was set to 8, 9, 10 or 11, minimum binding affinity fold change was set to 1, and downstream sequence length was set to full, with default parameters used for all other settings.

Downstream neoantigen analyses were performed using the pVACseq output linked to its respective mutation information. Neoantigen-causing mutations were defined as all mutations that gave rise to at least one neoantigen. The observed-to-expected neoantigen ratio was calculated using a previously developed approach that compares each tumour's observed neoantigen rate to an empirically derived expected rate that assumes no selection against neoantigen-causing mutations[39]: From the gold set samples in the GLASS cohort ($n = 222$), define $\overline{N_s}$ to be the expected number of nonsynonymous missense SNVs per synonymous SNV with trinucleotide context s. $\overline{B_s}$ is then defined as the expected number of neoantigen-generating missense SNVs per nonsynonymous missense SNV with trinucleotide context s. For a given sample i, define Y_i as the sample's set of synonymous SNVs and $s(m)$ to be a synonymous SNV with trinucleotide context m. The expected number of nonsynonymous missense SNVs, N_{pred}, and neoantigen-causing mutations, B_{pred}, can then be calculated as follows:

$$N_{\text{pred},i} = \sum_{m \in Y_i} \overline{N}_{s(m)}$$

$$B_{\text{pred},i} = \sum_{m \in Y_i} \overline{N}_{s(m)} \overline{B}_{s(m)}$$

To obtain the final neoantigen depletion ratio, R_i, of sample i, the observed number of neoantigen-causing mutations in the sample, $B_{\text{obs},i}$ is divided by the sample's observed number of nonsynonymous missense SNVs, $N_{\text{obs},i}$, and then this ratio is divided by the ratio of $B_{\text{pred},i}$ and $N_{\text{pred},i}$. Thus:

$$R_i = \frac{B_{\text{obs},i}/N_{\text{obs},i}}{B_{\text{pred},i}/N_{\text{pred},i}}$$

For analyses examining clonal/subclonal neoantigen ratios, the observed and expected numbers were calculated by subsetting the SNVs of a sample by the respective criteria and then recalculating the ratio as described above. To mitigate overfitting, all analyses presented here used samples from patients with at least three neoantigen-causing mutations in their primary and recurrent tumours.

Immune cell analyses

CIBERSORT relative immune cell fraction data used in downstream neoantigen analyses were downloaded from a previous publication[38].

Statistical methods

All data analyses were conducted in R 3.4.2, Python 2.7.15, PostgreSQL 10.5, and Julia 0.7. All survival analyses including Kaplan–Meier plots and Cox proportional hazards models were conducted using the R packages survival and survminer.

Reporting summary

Further information on research design is available in the Nature Research Reporting Summary linked to this paper.

Data availability

All de-identified, non-protected access somatic variant profiles and clinical data are accessible via Synapse (http://synapse.org/glass). Raw data of the various sequencing datasets can be obtained in the Supplementary Information.

Code availability

All custom scripts and pipelines are available on the project's github page (https://github.com/TheJacksonLaboratory/GLASS).

48. Brennan, C. W. et al. The somatic genomic landscape of glioblastoma. *Cell* **155**, 462–477 (2013).
49. Droop, A. et al. How to analyse the spatiotemporal tumour samples needed to investigate cancer evolution: a case study using paired primary and recurrent glioblastoma. *Int. J. Cancer* **142**, 1620–1626 (2018).
50. Mazor, T. et al. DNA methylation and somatic mutations converge on the cell cycle and define similar evolutionary histories in brain tumors. *Cancer Cell* **28**, 307–317 (2015).
51. Kim, J. et al. Spatiotemporal evolution of the primary glioblastoma genome. *Cancer Cell* **28**, 318–328 (2015)
52. Suzuki, H. et al. Mutational landscape and clonal architecture in grade II and III gliomas. *Nat. Genet*. **47**, 458–468 (2015).
53. Köster, J. & Rahmann, S. Snakemake—a scalable bioinformatics workflow engine. *Bioinformatics* **34**, 3600 (2018).
54. Van der Auwera, G. A. et al. From FastQ data to high confidence variant calls: the Genome Analysis Toolkit best practices pipeline. *Curr. Protoc. Bioinformatics*. **43**, 11.10.11–11.10.33 (2013).
55. Ewels, P., Magnusson, M., Lundin, S. & Käller, M. MultiQC: summarize analysis results for multiple tools and samples in a single report. *Bioinformatics* **32**, 3047–3048 (2016).
56. Li, H. et al. The Sequence Alignment/Map format and SAMtools. *Bioinformatics* **25**, 2078–2079 (2009).
57. Mermel, C. H. et al. GISTIC2.0 facilitates sensitive and confident localization of the targets of focal somatic copy-number alteration in human cancers. *Genome Biol*. **12**, R41 (2011).
58. Beroukhim, R. et al. Assessing the significance of chromosomal aberrations in cancer: methodology and application to glioma. *Proc. Natl Acad. Sci. USA* **104**, 20007–20012 (2007).
59. Taylor, A. M. et al. Genomic and functional approaches to understanding cancer aneuploidy. *Cancer Cell* **33**, 676–689.e673 (2018).
60. Roth, A. et al. PyClone: statistical inference of clonal population structure in cancer. *Nat. Methods* **11**, 396–398 (2014).
61. Turajlic, S. et al. Tracking cancer evolution reveals constrained routes to metastases: TRACERx Renal. *Cell* **173**, 581–594.e512 (2018).
62. Ha, G. et al. TITAN: inference of copy number architectures in clonal cell populations from tumor whole-genome sequence data. *Genome Res*. **24**, 1881–1893 (2014).
63. Szolek, A. et al. OptiType: precision HLA typing from next-generation sequencing data. *Bioinformatics* **30**, 3310–3316 (2014).
64. Hoof, I. et al. NetMHCpan, a method for MHC class I binding prediction beyond humans. *Immunogenetics* **61**, 1–13 (2009).

Acknowledgements This work is made possible by the patients and their families whom generously contributed to this study. This work is supported by the National Brain Tumor Society, Oligo Research Fund; Cancer Center Support grants P30CA16672 and P30CA034196; Cancer Prevention & Research Institute of Texas (CPRIT) grant number R140606; Agilent Technologies (R.G.W.V.); the National Institutes of Health- National Cancer institute for the following grants: NCI CA170278 (L.M.P., T.M.M., H.N.), NCI R01CA222146 (L.M.P., H.K.N.), NCI R01CA230031 (J.H.C., J.N.), NCI R01CA188288 (J.S.B.-S., R.B., P.B., K.L.L., A. Chakravarty., A.E.S.), R01CA179044 (A. Iavarone), U54CA193313 (A. Iavarone). The National Brain Tumor Society (W.K.A.Y., J.F.d.G.). Brain Tumour Northwest tissue bank (including the Walton research tissue bank) is supported by the Sidney Driscol Neuroscience Foundation and part of the Walton Centre and Lancashire Teaching Hospitals NHS Foundation Trusts (A.F.B., M.D.J.). This work was supported by a generous gift from the Dabbiere family (J.F.C.). Support is also provided by a Leeds Charitable Foundation grant (9R11/14-11 to L.F.S.), University of Leeds Academic Fellowship (11001061) (L.F.S.) and Studentship (11061191) (G. Tanner) as well as Leeds Teaching Hospitals NHS Trust (A. Chakravarti, A. Ismail). The Leeds Multidisciplinary Research Tissue Bank staff was funded by the PPR Foundation and The University of Leeds (S.C.S.). Funds were received from The Brain Tumour Charity (C.W., grants 10/136 & GN-000580, B.A.W., 200450). Ghazaleh Tabatabai is funded by EKFS 2015_Kolleg_14. R01CA218144 (P.S.L., E.J.C., J.C., A.K.L.) and Strain for the Brain, Milwaukee, WI (P.S.L., E.J.C., J.C., A.K.L.). E.K. is recipient of an MD-Fellowship by the Boehringer Ingelheim Fonds and is supported by the German National Academic Foundation. The Leeds Multidisciplinary Research Tissue Bank staff was funded by the PPR Foundation and part of the University of Leeds (S.C.S.). GLASS-Austria was funded by the Austrian Science Fund project KLI394 (A.W.). GLASS-Germany was funded by the German Ministry of Education and Research (BMBF) 031A425 (G. Reifenberger, P.L.) and German Cancer Aid (DKH) 70-3163-Wi 3 (M.W.). GLASS-NL receives support from KWF/Dutch Cancer Society project 11026 (M.C.M.K., P.W., R.G.W.V., P.J.F., J.M.N., M. Smits, B.A.W.). We thank the University of Colorado Denver Central Nervous System Biorepository (D.R.O.) for providing tissue samples. Sponsoring was also received from the National Institute of Neurological Disorders and Stroke (NINDS R01NS094615, G. Rao), F.S.V. is supported by a postdoctoral fellowship from The Jane Coffin Childs Memorial Fund for Medical Research. F.P.B. is supported by the JAX Scholar program and the National Cancer Institute (K99 CA226387); K.C.J. is the recipient of an American Cancer Society Fellowship (130984-PF-17-141-01-DMC). We thank the Jackson Laboratory Clinical and Translation Support team for coordinating all data transfer agreements. We thank M. Wimsatt for assistance in graphic design.

Author contributions Sequencing data coordination was performed by H.K., F.P.B. and K.C.J., and clinical data coordination was by A.D.M. and O.A. Data analysis was led by F.P.B. and K.C.J. in collaboration with K.J.A., S.B.A., J.H.C., H.K., E.K., J.N., L.F.S., G. Tanner, F.S.V. and R.G.W.V. Clinical analysis was performed by F.P.B., K.C.J., A.D.M., L.M.P. and C.W. Pathology review was completed, in part, by A. Chakrabarty, J.T.H., A. Ismail, A.W, H.K.N., K.L.L., G. Reifenberger and K.A. F.P.B., K.C.J., A.D.M., F.S.V. and R.G.W.V. wrote the manuscript. K.D.A., J.H. and J.F.d.G. coordinated the GLASS-MDACC cohort. L.F.S. was the lead coordinator of the GLASS-Leeds cohort and B.A.W. the lead coordinator of GLASS-Netherlands. D.M.A., D.A., P.B., J.S.B.-S., R.B., C.B., P.K.B., D.J.B., A.R.B. A. Chakrabarty, A. Chakravarti, E.J.C., J.F.C., G.F., M.N.F., A. Iavarone, M.D.J., M.K., P.S.L., M.L., P.L., K.L.L., T.M.M., T.M., A.M.M., D.-H.N., N.N., H.K.N., C.Y.N., S.P.N., H.N., D.R.O., C.-K.P., L.M.P., G. Rao, B.R., J.K.S., S.C.S., A.E.S., M. Schuster, L.F.S., H.S., E.G.V.M., C.W., M.W., G.W. and A.W. contributed to sample acquisition and processing. All co-authors including K.A., P.B., A.F.B., K.R.B., E.B.C., J.C., P.J.F., H.K.G., M. R. Grimmer, P.V.G., M. R. Gilbert, A.K.L., K.L.M., J.M.N., R.R., G. Reifenberger, B.L.S., P.A.S.S., M. Smits, G. Tabatabai, P.W., W.K.A.Y. and G.Z. discussed the results and commented on the manuscript and Supplementary Information. R.G.W.V. was the project lead and coordinator.

Competing interests R.G.W.V. declares equity in Boundless Bio, Inc. M.K. receives research grants from BMS and ABBVie. P.K.B. is a consultant for Lilly, Genentech-Roche, Angiochem and Tesaro. P.K.B. receives institutional funding from Merck and Pfizer and honoraria from Merch and Genentech-Roche. W.K.A.Y. serves in a consulting or advisory role at DNAtrix Therapeutics. M.W. receives funding from Acceleron, Actelion, Bayer, Isarna, Merck, Sharp & Dohme, Merck (EMD, Darmstadt), Novocure, OGD2, Pigur and Roche as well as honoraria from BMS, Celldex, Immunocellular Therapeutics, Isarna, Magforce, Merck, Sharp & Dohme, Merck (EMD, Darmstadt), Northwest Biotherapeutics, Novocure, Pfizer, Roche, Teva and Tocagen. G. Reifenberger receives funding from Roche and Merck (EMD, Darmstadt) as well as honoraria from AbbVie. M. Smits is a central reviewer for Parexel Ltd and honoraria are paid to the institution. G. Tabatabai reports personal fees from Bristol-Myers-Squibb, personal fees from AbbVie, personal fees from Novocure, personal fees from Medac, travel grants from Bristol-Myers-Squibb, education grants from Novocure, research grants from Roche Diagnostics, research grants from Medac, membership in the National Steering board of the TIGER NIS (Novocure) and the International Steering board of the ON-TRK NIS (Bayer).

Additional information

Supplementary information is available for this paper at https://doi.org/10.1038/s41586-019-1775-1.

Correspondence and requests for materials should be addressed to R.G.W.V.

Peer review information *Nature* thanks Kamila Naxerova, Wolfgang Wick and the other, anonymous, reviewer(s) for their contribution to the peer review of this work.

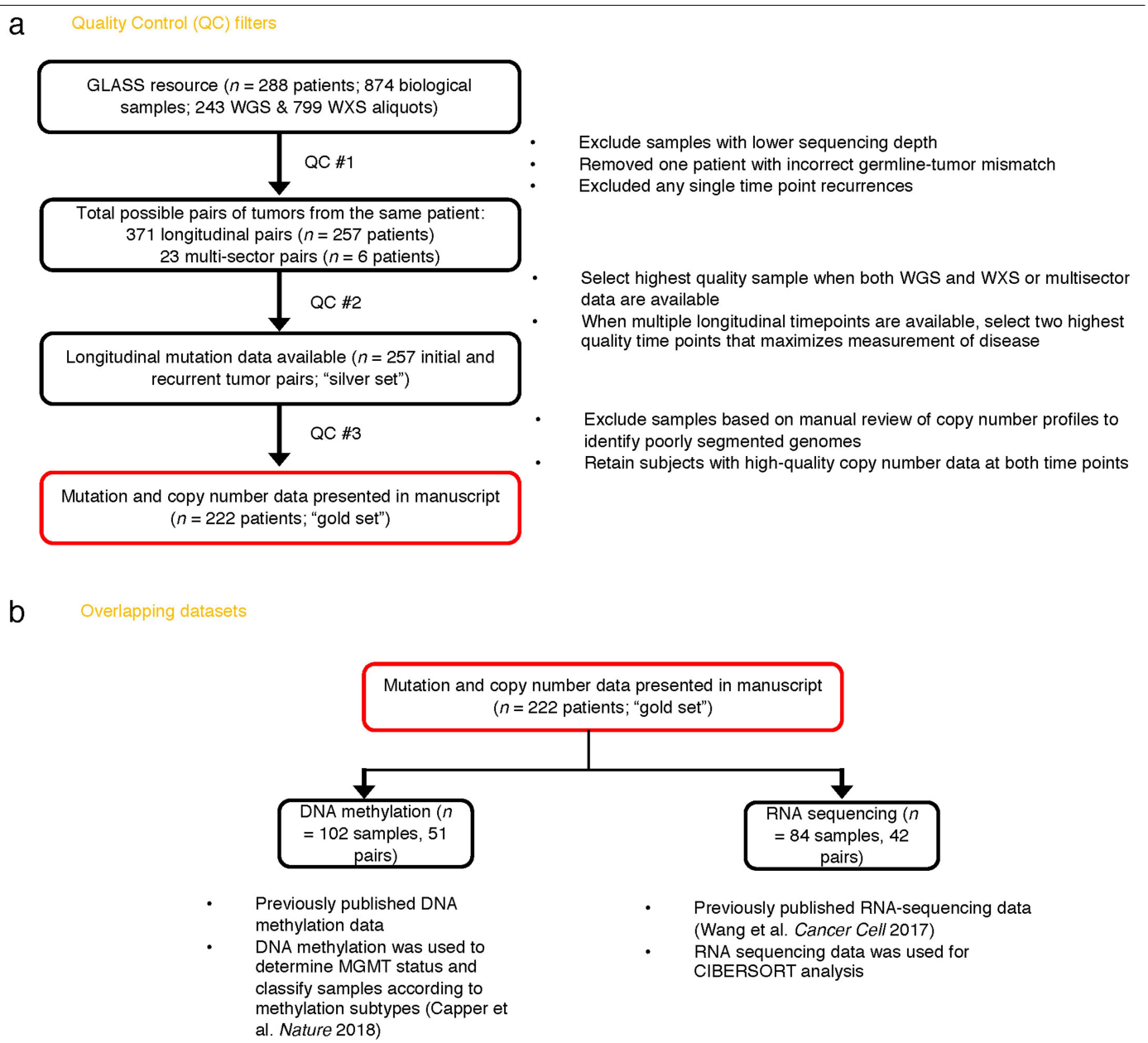

Extended Data Fig. 1 | Sample selection. a, Quality control workflow steps identifying all GLASS samples available as a resource and the identification of the highest quality set of patient pairs ($n = 222$) used for the presented mutational and copy number analyses. **b**, Additional available datasets.

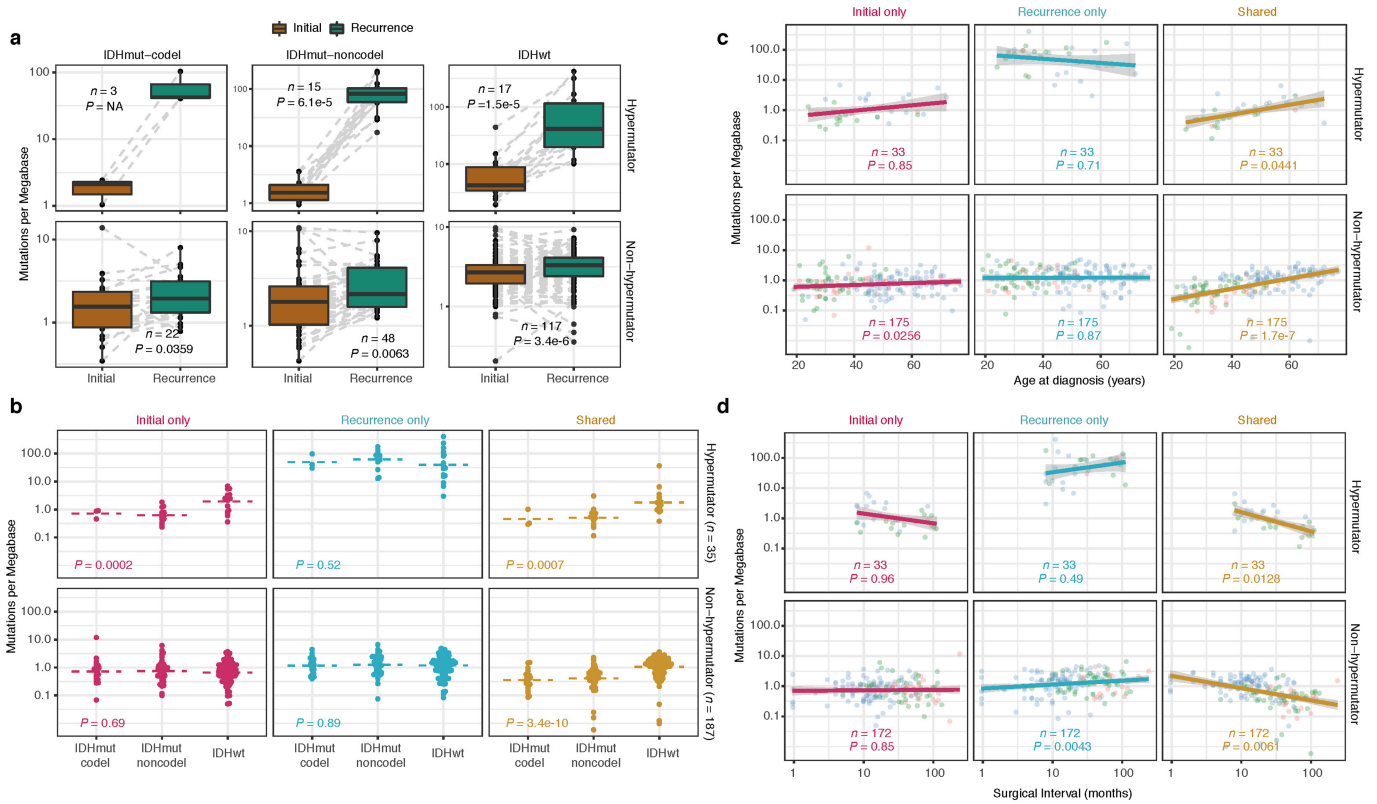

Extended Data Fig. 2 | Mutation burden by time point and subtype. a, Box plots and paired lines depicting coverage-adjusted mutation frequencies in initial and matched recurrent samples across three subtypes. Wilcoxon signed-rank test *P* values and sample sizes are indicated. **b**, Bee swarm plot depicting coverage-adjusted mutation frequencies in fractions by subtype. Dashed line indicates the mean. *P* values comparing three subtypes were determined by one-way analysis of variance (ANOVA). **c**, Scatter plot showing the relationship between age at diagnosis and coverage adjusted mutation burdens by subtype and fraction. *P* values were determined by the linear model and adjusted by subtype. **d**. Similar to the analysis in **c** but showing the relationship between time to recurrence and coverage-adjusted mutation burdens.

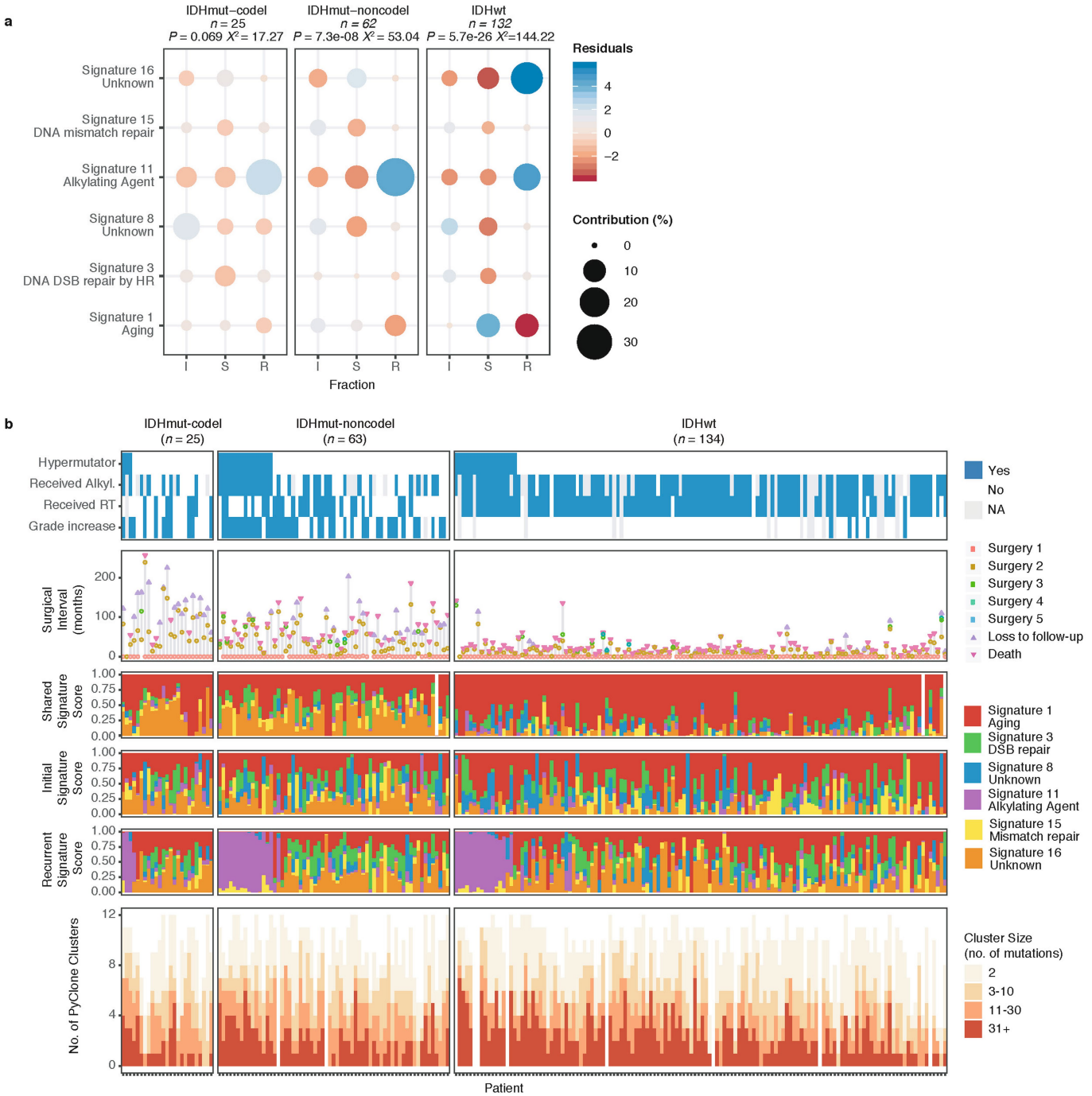

Extended Data Fig. 3 | Mutational signatures by fraction and subtype. **a**, Correlation plot showing the Pearson's chi-squared (χ^2) residuals for each signature by fraction and subtype. A χ^2 test was performed for each subtype and *P* values are indicated. Positive residuals (blue) indicate a positive correlation, whereas negative residuals (red) indicate an anti-correlation. The point size reflects the contribution to the χ^2 estimate. **b**, Patients were ordered as in Fig. 1a, and relevant clinical information is provided alongside the fraction-specific mutational signatures. PyClone mutational clusters are also presented.

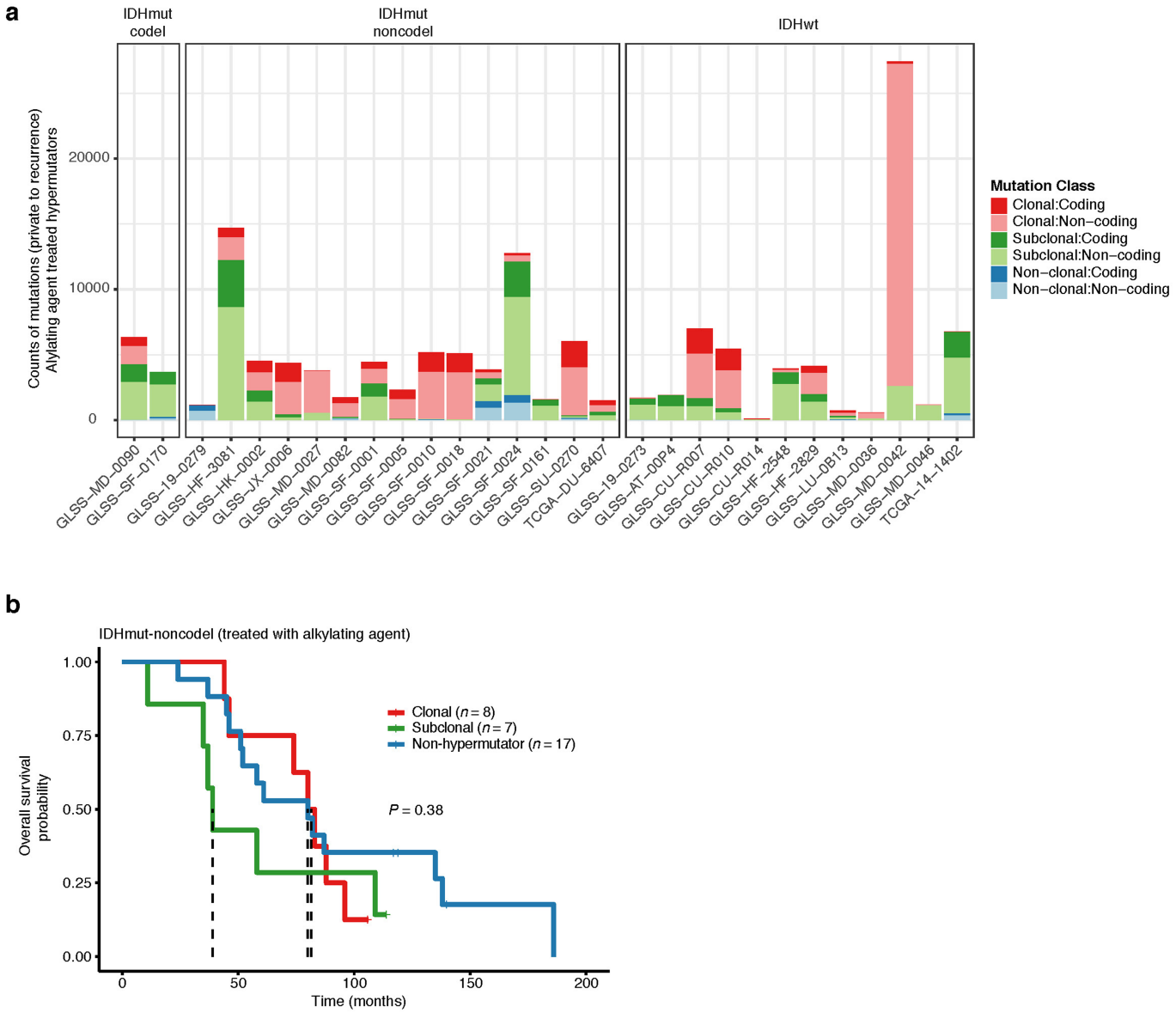

Extended Data Fig. 4 | Hypermutator clonality. a, Bar plots represent counts of recurrence-only mutations per hypermutator tumour that were known to receive treatment alkylating agent and were successfully run through the PyClone algorithm. Colours indicate mutation clonality and colour intensity indicates whether the mutations resulted in coding changes. **b**, Kaplan–Meier curve comparing the survival of alkylating agent-treated IDH-mutant-noncodel hypermutator tumours that were predominantly clonal ($n = 8$), predominantly subclonal ($n = 7$) or non-hypermutator ($n = 17$). Limited to tumours with available PyClone data. *P* value determined by log-rank test.

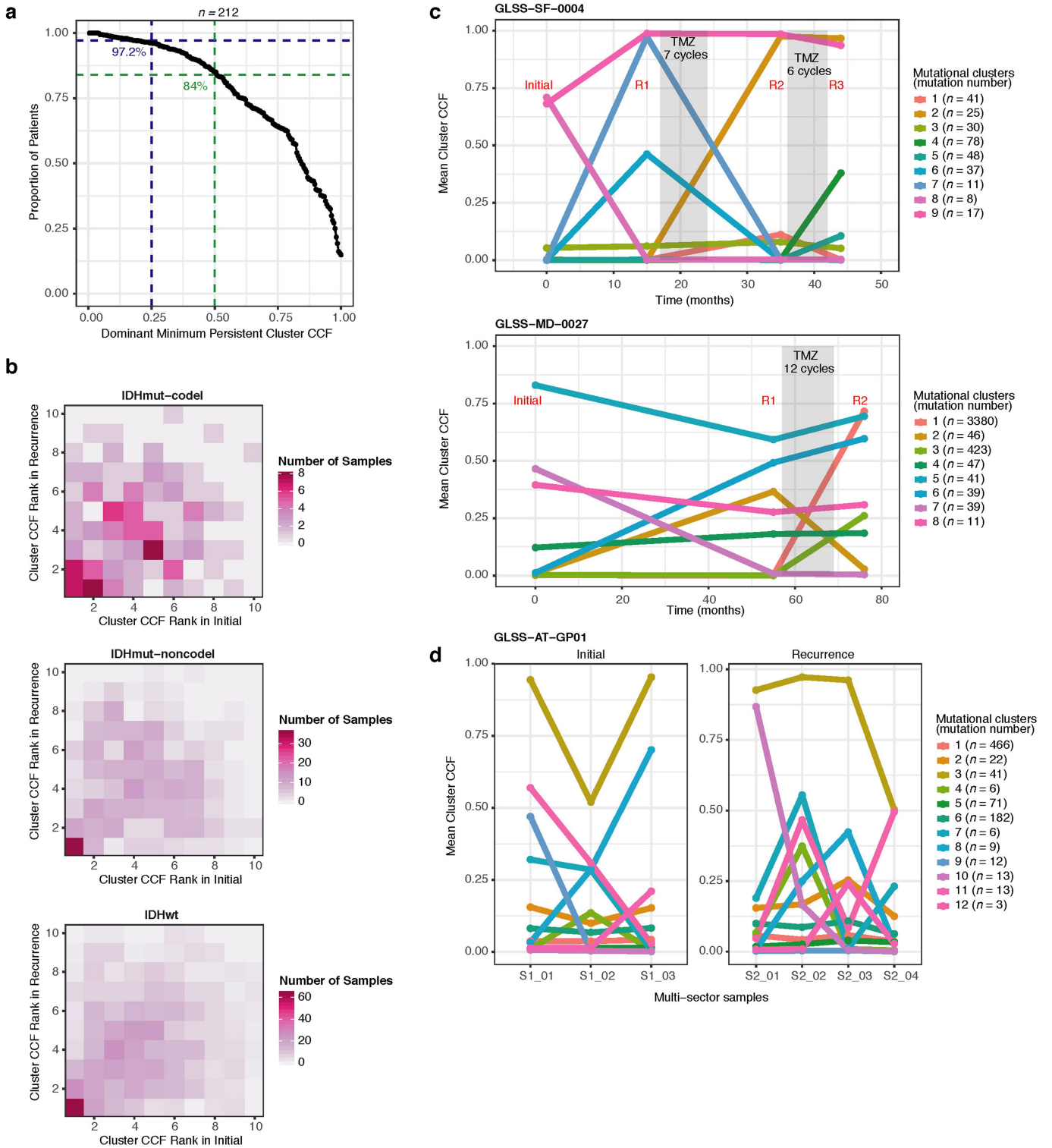

Extended Data Fig. 5 | Clonal structure evolution over time. a, The minimum CCF of the most persistent (shared between initial and recurrence) PyClone cluster. **b**, Comparison of PyClone clusters ranked by CCF in matched initial and recurrent tumours, as in Fig. 2b, but separated by subtype. **c**, **d**, Examples of cluster CCF dynamics over time in three separate samples, including two multi-time point samples (**c**) and one multi-sector sample (**d**). These additional data are available in the GLASS resource, but only two time-separated samples were used throughout to ensure clarity.

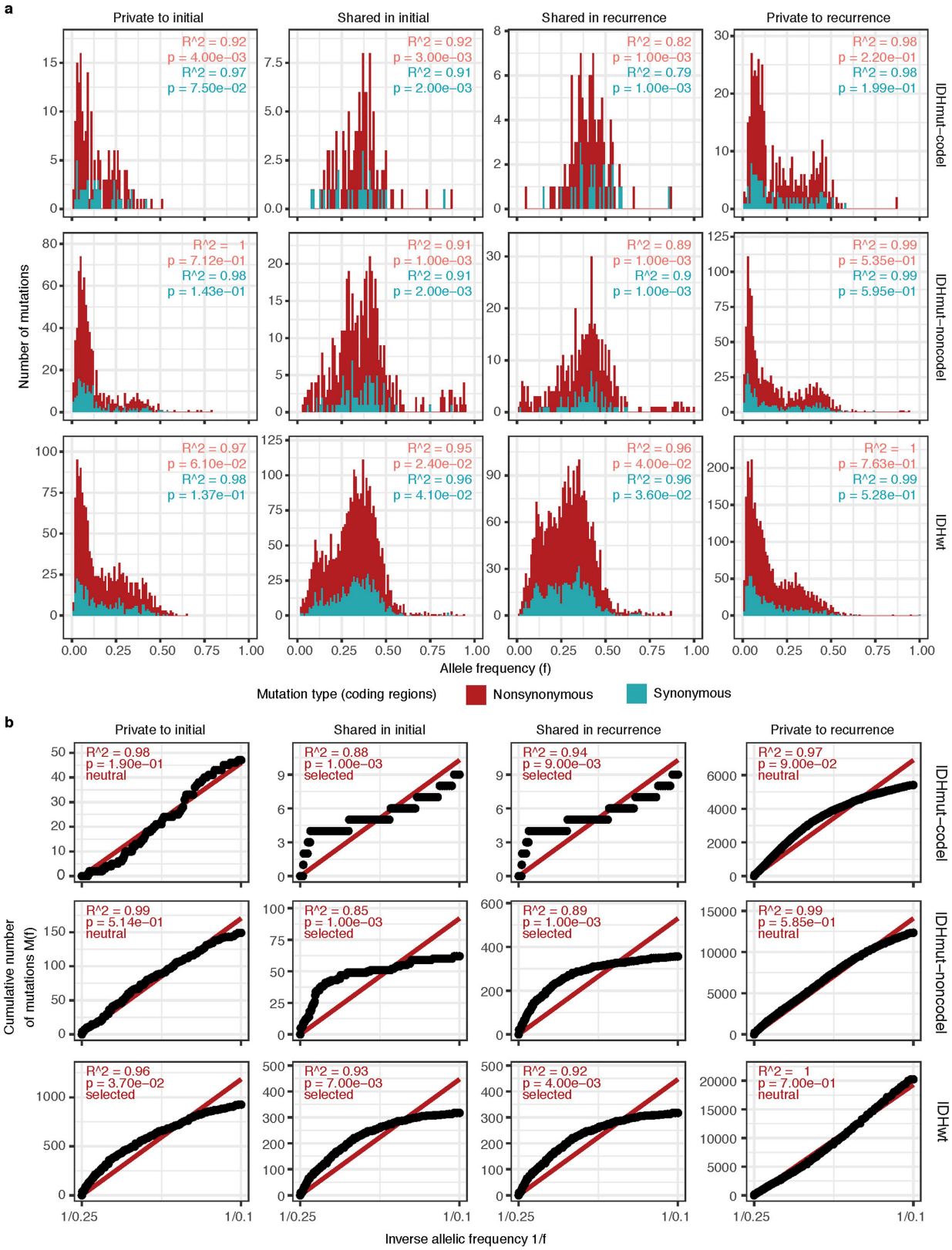

Extended Data Fig. 6 | Distribution of variant allele fraction. a, Distributions of non-hypermutator variant allele fraction for copy-neutral variants in coding regions ($n = 181$ patients). Variants are separated by subtype, fraction and also the variant was non-synonymous or synonymous mutation in a coding region. R^2 goodness-of-fit measure and associated P values are shown. Note that these data consider only the coding portion of genome, whereas Fig. 2d presents both coding and non-coding data. **b**, The cumulative distribution of the subclonal mutations in copy-neutral regions for hypermutators ($n = 31$ patients). For each variant fraction and subtype, the R^2 goodness-of-fit measure and P values are shown.

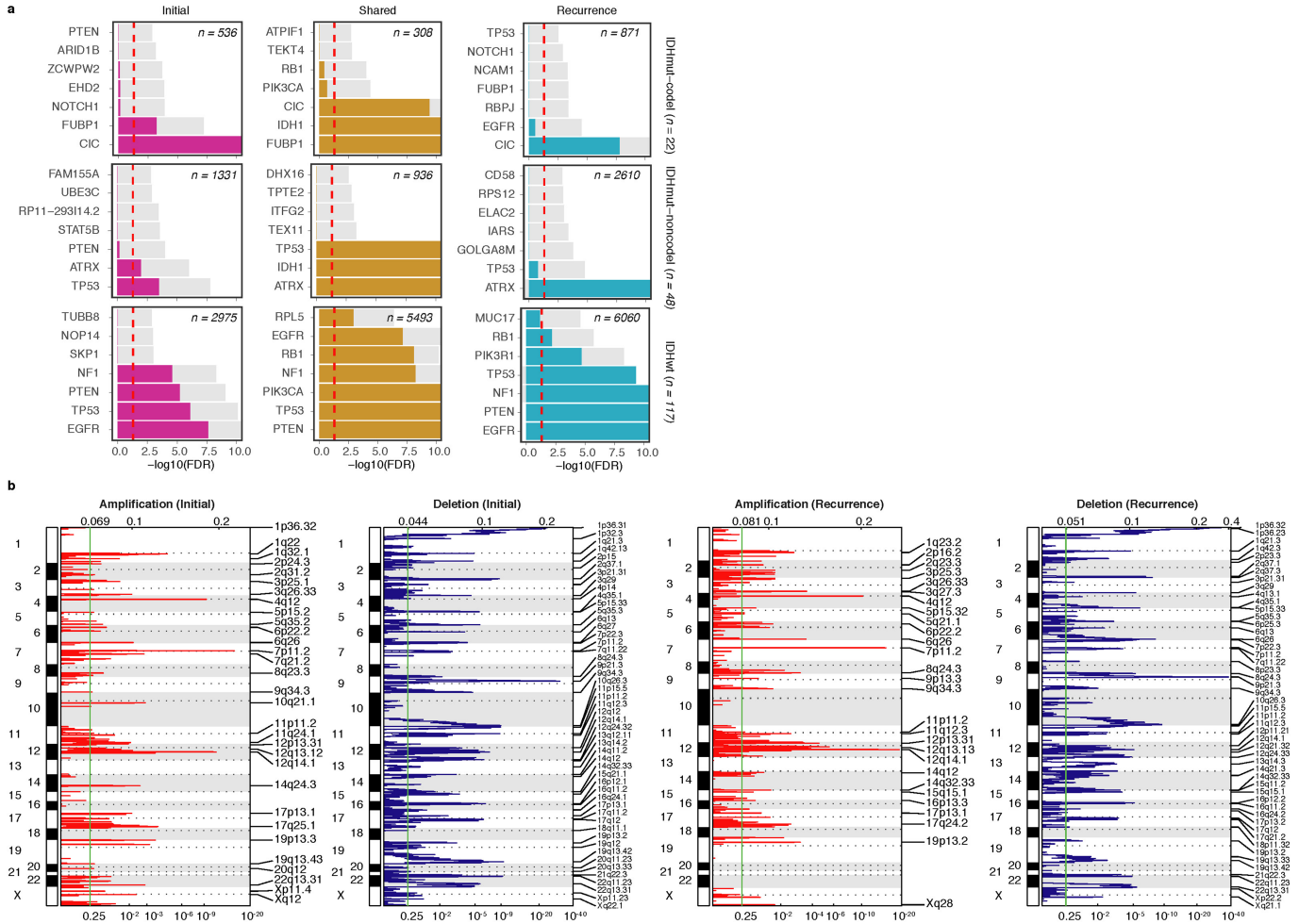

Extended Data Fig. 7 | Driver gene nomination. a, Local (gene-wise) dN/dS estimates by subtype (rows) and fraction (columns). Genes are sorted by *Q* value and *P* value. The *Q* value is shown in colour, whereas the *P* value is indicated in light grey. The *Q* value threshold of 0.05 is indicated by a horizontal red line. **b**, GISTIC significant amplification (red) and deletion (blue) plots in initial (left) and recurrent tumours (right). Chromosomal locations are ordered on the *y* axis, *Q* values are shown on the *x* axis, and selected drivers are indicated by their chromosomal location on the right.

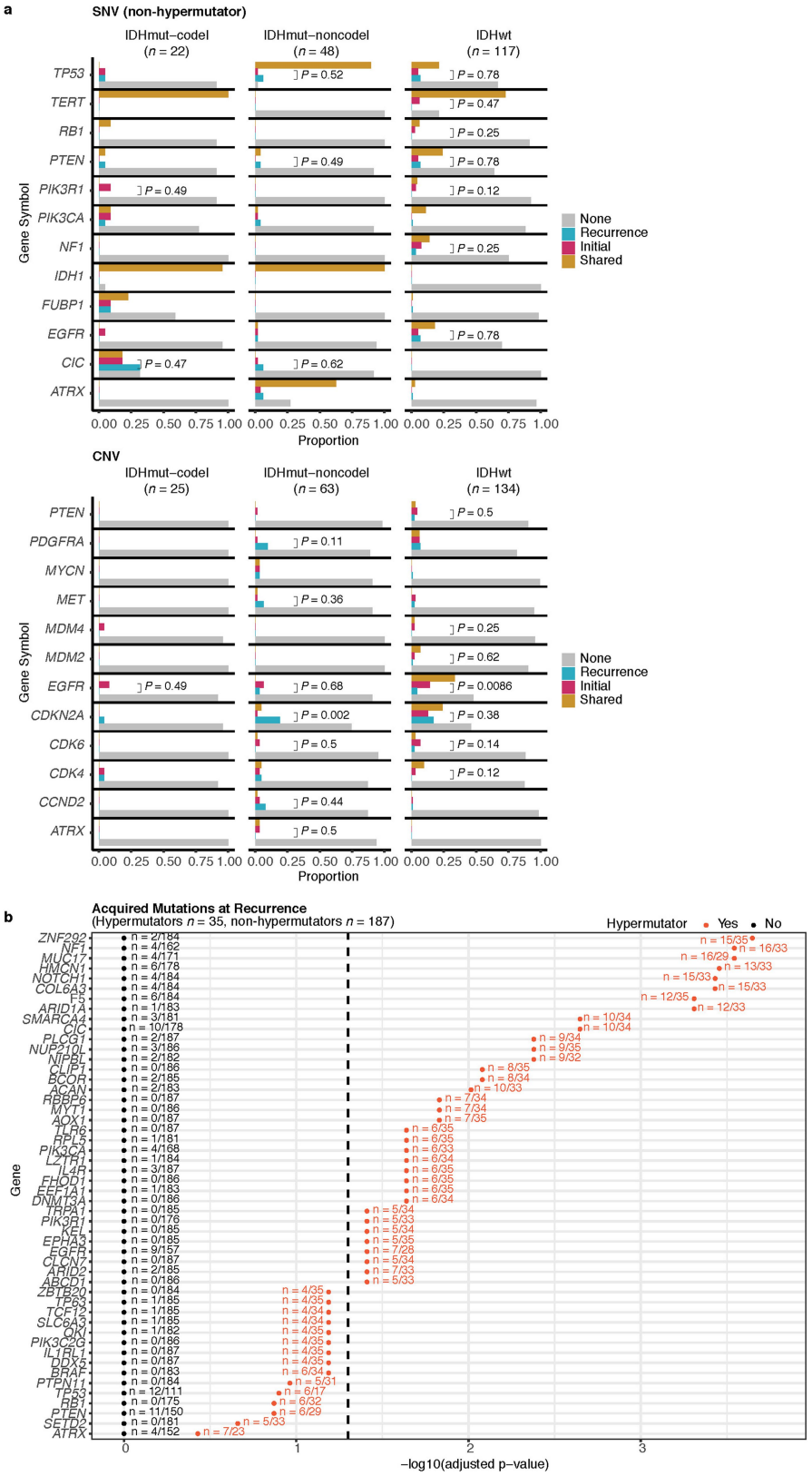

Extended Data Fig. 8 | Driver acquisition over time. a, Tabulated numbers of SNV (top) and CNV (bottom) driver events that were shared, initial-only or recurrence-only. *P* values were determined by a two-sided Fisher test comparing the initial-only fraction to the recurrence-only fraction testing for acquisition. **b**, One-sided Fisher test comparing the initial-only fraction to the recurrence-only fraction among previously implicated glioma drivers testing for driver acquisition. *P* values were adjusted for multiple testing using the false discovery rate (*x* axis). Hypermutators (red) and non-hypermutators (black) were separately analysed.

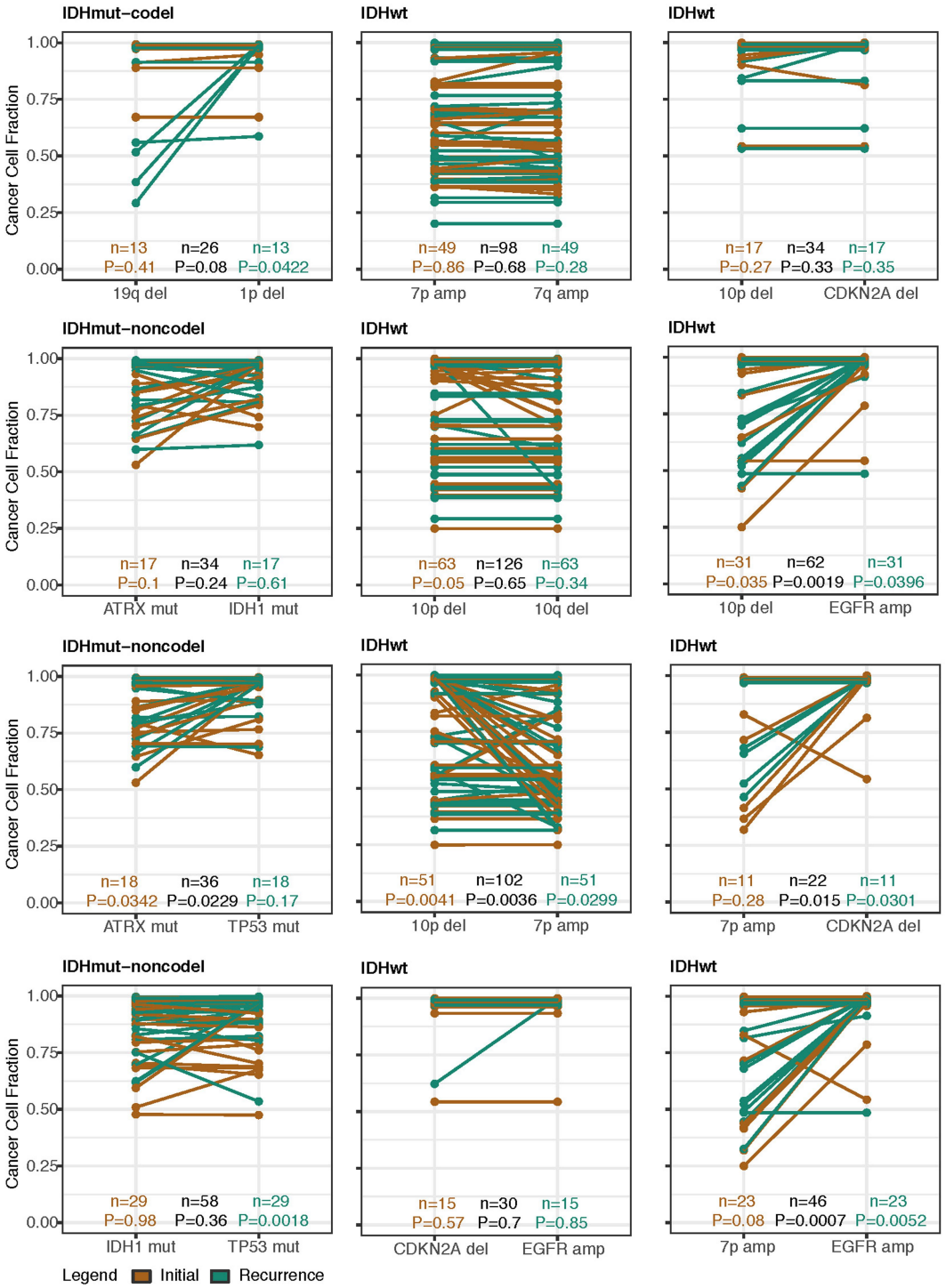

Extended Data Fig. 9 | Intra-tumour CCF comparison. Ladder plots comparing the CCF of co-occurring drivers in single tumour samples. The colour of the lines and points indicates whether the sample shown is an initial (brown) or recurrent (green) tumour. *P* values determined by two-sided Wilcoxon rank-sum test for all initial samples, recurrent samples, as well as all samples (black).

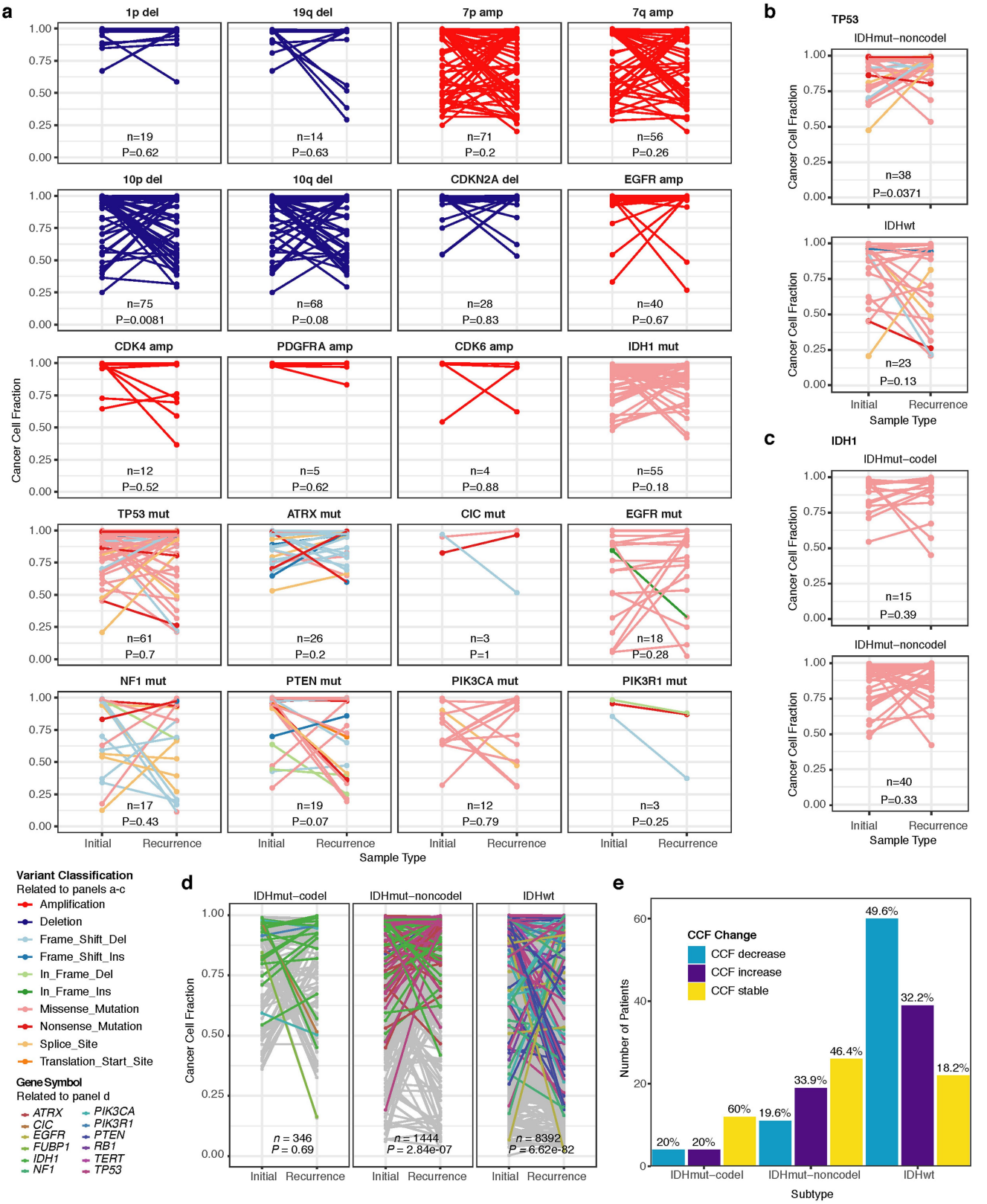

Extended Data Fig. 10 | Between time point intra-patient CCF comparison. **a**, Driver gene CCF comparison between initial and matched recurrences. Lines are coloured by variant classification. *P* values determined by two-sided Wilcoxon rank-sum test. **b**, *TP53* CCF by subtype, otherwise as in **a**. **c**, *IDH1* CCF by subtype, otherwise as in **a**. **d**, Ladder plot visualizing change in CCF across all SNVs between initial and recurrent tumours, separated by subtype. *P* values determined by Wilcoxon rank-sum test. **e**, Initial and recurrent mutations in each patient were compared using a Wilcoxon rank-sum test. Bar plot with counts of patients in each subtype are shown. Patients lacking significant change are shown in yellow, and those with a significant increase or decrease are shown in dark and light blue, respectively.

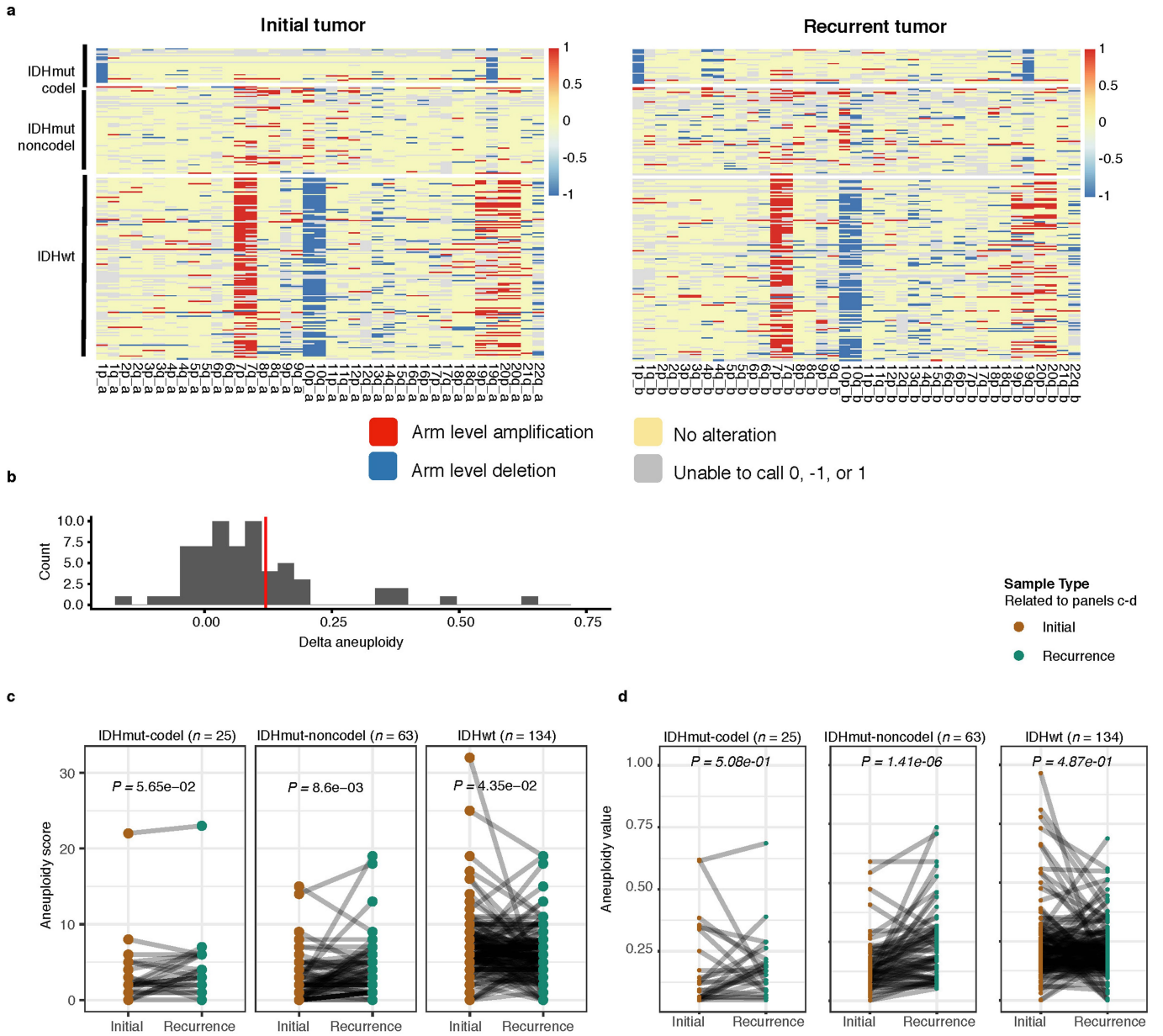

Extended Data Fig. 11 | Aneuploidy calculation. a, Heat map displaying the chromosomal arm-level events (*x* axis) with patients represented in each row. Patients are placed in the same order for both the initial (left) and recurrence (right). White space was inserted as a break between the three subtypes. **b**, Distribution of total aneuploidy difference. Acquired aneuploidy determination (upper-quartile) indicated with a red line. **c**, Comparison of aneuploidy score between initial and recurrent tumours separated by subtype **d**. As in **c**, comparing aneuploidy value.

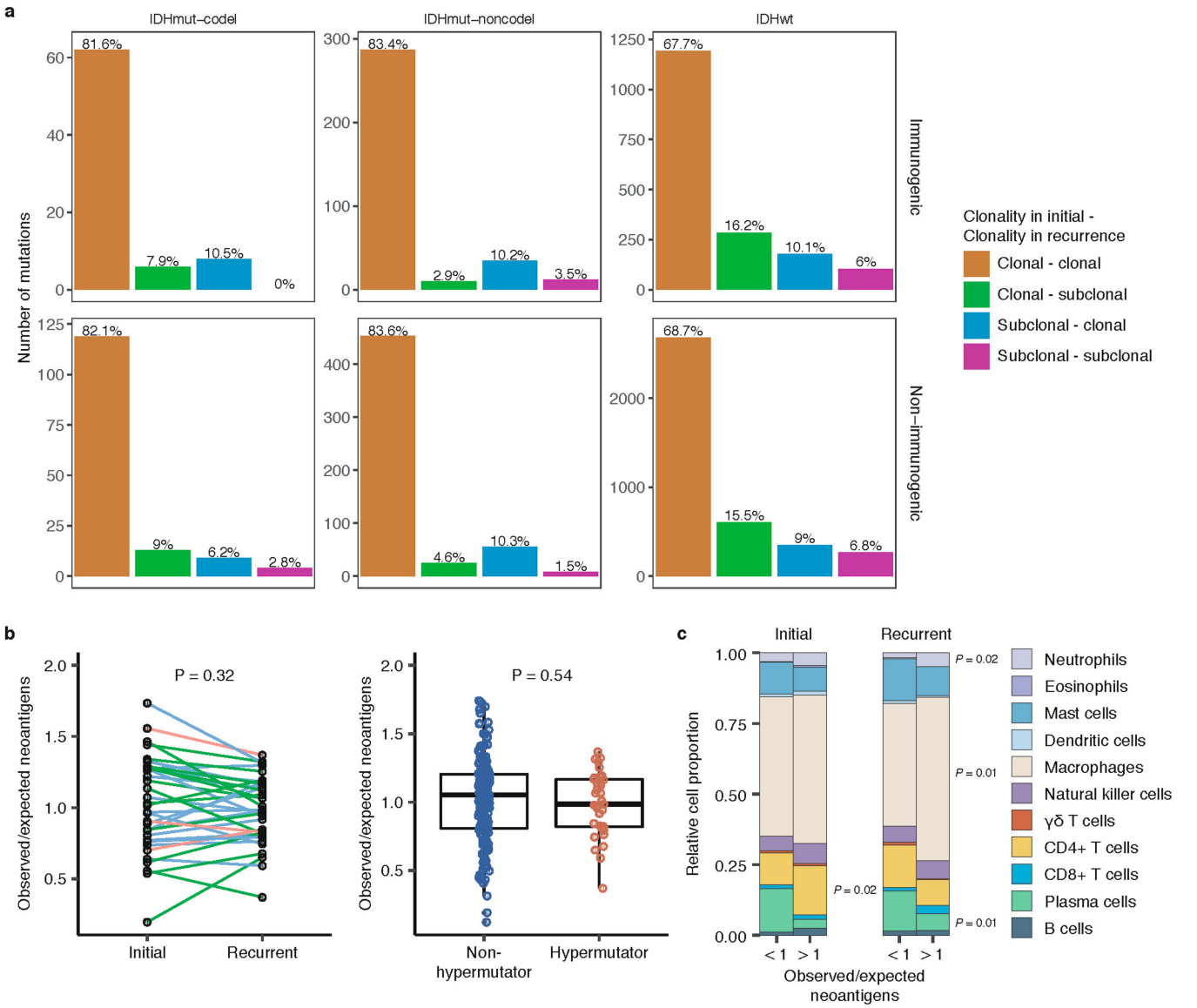

Extended Data Fig. 12 | Neoantigen evolution and cellular analysis. a, Bar plots representing the number of shared mutations that give rise to neoantigens (top row, 'immunogenic') and those that do not give rise to neoantigens (bottom row, 'non-immunogenic') stratified by longitudinal clonality ('(clonality in initial) – (clonality in recurrence)') and further separated by subtype. The percentage of longitudinal clonality per subtype and mutation is shown. **b**, Left, ladder plot depicting the difference in observed-to-expected neoantigen ratio between the initial and recurrent tumours of patients with hypermutated tumours at recurrence. Each set of points connected by a line represents one tumour ($n = 70$). Right, box plot depicting the distribution of observed-to-expected neoantigen ratios in recurrent tumours stratified by hypermutator status ($n = 35$ and 183 for hypermutators and non-hypermutators, respectively). Each box spans quartiles, with the lines representing the median ratio for each group. Whiskers represent absolute range, excluding outliers. *P* values were determined by a paired and an unpaired two-sided *t*-test, for left and right graphs, respectively. **c**, Stacked bar plots depicting the average relative fraction of 11 CIBERSORT cell types in the neoantigen depleted (<1) and non-depleted (>1) initial and recurrent tumour subgroups. *P* values to the right of each plot indicate a significant difference between the depleted and non-depleted groups for the noted cell type at that time.

nature research

Corresponding author(s): Roel GW Verhaak

Last updated by author(s): Sept. 09, 2019

Reporting Summary

Nature Research wishes to improve the reproducibility of the work that we publish. This form provides structure for consistency and transparency in reporting. For further information on Nature Research policies, see Authors & Referees and the Editorial Policy Checklist.

Statistics

For all statistical analyses, confirm that the following items are present in the figure legend, table legend, main text, or Methods section.

n/a	Confirmed	
☐	☒	The exact sample size (*n*) for each experimental group/condition, given as a discrete number and unit of measurement
☐	☒	A statement on whether measurements were taken from distinct samples or whether the same sample was measured repeatedly
☐	☒	The statistical test(s) used AND whether they are one- or two-sided *Only common tests should be described solely by name; describe more complex techniques in the Methods section.*
☐	☒	A description of all covariates tested
☐	☒	A description of any assumptions or corrections, such as tests of normality and adjustment for multiple comparisons
☐	☒	A full description of the statistical parameters including central tendency (e.g. means) or other basic estimates (e.g. regression coefficient) AND variation (e.g. standard deviation) or associated estimates of uncertainty (e.g. confidence intervals)
☐	☒	For null hypothesis testing, the test statistic (e.g. *F*, *t*, *r*) with confidence intervals, effect sizes, degrees of freedom and *P* value noted *Give P values as exact values whenever suitable.*
☒	☐	For Bayesian analysis, information on the choice of priors and Markov chain Monte Carlo settings
☒	☐	For hierarchical and complex designs, identification of the appropriate level for tests and full reporting of outcomes
☐	☒	Estimates of effect sizes (e.g. Cohen's *d*, Pearson's *r*), indicating how they were calculated

Our web collection on statistics for biologists contains articles on many of the points above.

Software and code

Policy information about availability of computer code

Data collection	No software was used for data collection.
Data analysis	MultiQC version: 1.6a0 (quality assessment) FastQC 0.11.7 (quality assessment) BWA MEM 0.7.17 (alignment) R 3.4.2 (general data analyses) Python 2.7.15 (general data analysis) Julia 0.7 (general data analysis) PostgreSQL 10.5 (data management) BCFTools 1.9 (normalize, sort and index variants) snakemake 5.2.2 (pipeline development) GATK (including Mutect2) version: 4.1.0.0 (SNV/CNV detection) freebayes version: 1.2.0 (variant filtering) vcf2maf version: 1.6.16 (variant filtering and annotation) MutationalPatterns version: 1.6.1 (mutational signatures) TITAN version: 1.19.1 (purity, ploidy, CNV clonality estimates) dndscv (R package) version: 0.0.1.0 (selection strength, nominate driver genes) alluvial (R package) version: 0.1-2 (visualize longitudinal neutrality) DBI (R package) version: 1.0.0 (database management) tidyverse (R package) version: 1.2.1 (data analysis and visualization) survival (R package) version: 2.42-6 (survival analyses) neutralitytestr version: 0.0.2 (subtype-level, variant-level selection) SubClonalSelection version: 0.0.0 (sample-level selection) PyClone version: 0.13.1 (mutational clusters) OptiType version: 1.3.1 (HLA class I type) pVACseq version: 4.0.10 (neoantigen prediction) netMHCpan version: 2.8 (neoantigen prediction) All other custom scripts and pipelines are available on the project's github page (https://github.com/TheJacksonLaboratory/GLASS)

For manuscripts utilizing custom algorithms or software that are central to the research but not yet described in published literature, software must be made available to editors/reviewers. We strongly encourage code deposition in a community repository (e.g. GitHub). See the Nature Research guidelines for submitting code & software for further information.

Data

Policy information about availability of data

All manuscripts must include a data availability statement. This statement should provide the following information, where applicable:

- Accession codes, unique identifiers, or web links for publicly available datasets
- A list of figures that have associated raw data
- A description of any restrictions on data availability

All deidentified, non-protected access somatic variant profiles and clinical data are accessible via Synapse (http://synapse.org/glass). A subset of whole genome and whole exome sequencing data has been deposited in the National Center for Biotechnology Information's Sequencing Read Archive and/or the European Genome/Phenome Archive (EGA). Please see Supplementary Table 1 for availability and accession codes.

Field-specific reporting

Please select the one below that is the best fit for your research. If you are not sure, read the appropriate sections before making your selection.

☒ Life sciences ☐ Behavioural & social sciences ☐ Ecological, evolutionary & environmental sciences

For a reference copy of the document with all sections, see nature.com/documents/nr-reporting-summary-flat.pdf

Life sciences study design

All studies must disclose on these points even when the disclosure is negative.

Sample size	No statistical methods were used to predetermine sample size. Sample size was a function of availability.
Data exclusions	We defined a quality control process to integrate whole exome and whole genome sequencing data collected from multiple cohorts. As shown in Extended Data Fig. 1, two datasets, Silver and Gold, were constructed to be used for each major analysis type, SNV and CNV, respectively. The two criteria used are intended to provide quality classifications for samples across fingerprinting, coverage, copy number variation (CNV) data and clinical annotation.Fingerprinting was performed using CrosscheckFingerprints (Picard), the purpose of this is to check that all of the input files (readgroups, libraries, samples, files) belong to the same patient, to remove duplicated cases, unmatched samples, and samples of poor quality. Any evidence of mismatch rendered the samples “blocked”, otherwise the sample was annotated as “allow”. To ensure suitable coverage for mutation calling, samples with near 0 mutation frequency as well as those 2 standard deviations below the mean for either WGS or WXS were annotated as “block”. Samples were categorized as “allow”, “review”, or “block”. Copy number data were excluded via manual review of all selected copy number solutions. Manual review consisted of identifying whether data had an atypical or noisy segmentation profile. While we recognize that this strategy is not objective it proved to be an effective strategy for identifying poor performing samples. Insufficient signal, noisy signal, TITAN run fail and unexpected genome stability (little to no copy number changes observed suggesting low purity) were the main reasons for sample exclusion or review. Clinical data was another source of sample filtering. Exclusion of samples was mostly related to sample pairs where surgical interval was very short (1-2 months) and thus did not appear to be a true recurrence. Caution should be used when considering whether a sample represents a true recurrence as no standard set time limits exist. Categories for clinical data include “allow”, “interval 1 or less months”, “interval 2 or less months”, “different location” and “surgical indication” (including “further debulking”). Those interested in using the dataset for further analysis are encouraged to make their own judgments on the criteria they select. The Silver set is filtered to include those pairs with no fingerprinting mismatches and sufficient coverage and is made up of 257 pairs. The Gold set contains 222 pairs, which in addition to the previously mentioned criteria also contain acceptable CNV calls in both samples.
Replication	Replication was limited to select patient samples where both whole genome sequencing and whole exome sequencing was available. All attempts at replication were successful.
Randomization	There was no randomization in this study.
Blinding	All patient samples were deidentified and were assigned a study-specific barcode. Blinding was not relevant to our study since there was no randomization of groups.

Reporting for specific materials, systems and methods

We require information from authors about some types of materials, experimental systems and methods used in many studies. Here, indicate whether each material, system or method listed is relevant to your study. If you are not sure if a list item applies to your research, read the appropriate section before selecting a response.

Materials & experimental systems

n/a	Involved in the study
☒	☐ Antibodies
☒	☐ Eukaryotic cell lines
☒	☐ Palaeontology
☒	☐ Animals and other organisms
☐	☒ Human research participants
☐	☒ Clinical data

Methods

n/a	Involved in the study
☒	☐ ChIP-seq
☒	☐ Flow cytometry
☒	☐ MRI-based neuroimaging

Human research participants

Policy information about studies involving human research participants

Population characteristics	The dataset includes 271 sets of at least two time-separated tumor samples and 17 standalone recurrences. The majority of sets contain two tumor samples (n=246, 85%), with 19 (6.6%) three-tumor sample sets, three (1%) four-tumor sample sets, one (0.3%) with a total of five tumor samples and 17 (5.9%) standalone post-treatment tumor samples. Basic clinical information including age (years), gender, overall survival (months), tumor grade, and tumor histology was available for 90% (260/288) of patients and for 92% (536/584) of tumor samples of the dataset. Temozolomide and radiation treatment information was available for 68% of the cohort (399/584), data on other treatment modalities was available for 119 patients. Median age at diagnosis of GLASS patients in the IDHmut-noncodel and IDHmut-codel subtypes were both 34 years old and in the IDHwt group age at diagnosis was 53 years old. This is compared with 46 years for IDHmut-codels, 38 years for the IDHmut-noncodels and 59 years in the TCGA cohort respectively. Patients in our dataset were biased toward longer survival as 261 patients were deemed fit for surgical resection or biopsy at recurrence. Median survival for primary glioblastoma patients was 21 months (95% CI 19–23) in the GLASS cohort versus 15 months in historical cohorts. Patients in this cohort were predominantly treated at teaching/academic centers, which have been shown to be an independent predictive factor of longer survival compared with non-teaching/community hospital settings All other relevant patient demographics for the GLASS cohort are presented in the Supplement.
Recruitment	Informed consent was obtained from all study subjects as part of each institution's individual IRB.
Ethics oversight	All tissue source centers listed in Supplementary Table 1 obtained study approval by the corresponding institutional review board (IRB) and informed consent from all patients in the cohort. Data pooling at the Jackson Laboratory was performed under the oversight of the IRB at the Jackson Laboratory.

Note that full information on the approval of the study protocol must also be provided in the manuscript.

Clinical data

Policy information about clinical studies

All manuscripts should comply with the ICMJE guidelines for publication of clinical research and a completed CONSORT checklist must be included with all submissions.

Clinical trial registration	*NA.*
Study protocol	*NA.*
Data collection	*NA.*
Outcomes	*NA.*